Propagation of Acoustic Perturbations in Non-Uniform Ducts with Non-Uniform Mean Flow Using Eigen Analysis in General Curvilinear Coordinate Systems

Alexander G. Wilson

Institute of Sound and Vibration Research, University of Southampton, University Road, Southampton SO17 1BJ. Email: a.g.wilson@soton.ac.uk

Abstract

A new framework, Eigen Analysis in General Curvilinear Coordinates (EAGCC), is presented for internal propagation of linear acoustic flow disturbances through irregular but smoothly varying duct geometries and non-uniform but smoothly varying mean flows. The framework is based on an eigen analysis of the linearised Euler equations for a perfect gas formulated in a general curvilinear coordinate system. A series of test cases are studied, from a simple uniform cylindrical annular duct with uniform mean flow to an axially and circumferentially non-uniform duct with non-uniform mean flow, which together validate the method for acoustic propagation through non-uniform annular ducts and non-uniform but irrotational and homentropic mean flow: although the framework provides for rotational and non-homentropic mean flow, and for modelling vortical and entropic flow perturbations, these features are not validated in this paper. Two propagation methods are presented. The first is a one-way "single sweep" calculation, in which only information travelling in the direction of propagation is retained. The second is an iterative "two-way sweep" method that accurately captures reflected waves and returns transmitted and reflected perturbations. Previous eigenvector analyses were subject to limitations on geometry and mean flow (for instance slowly-varying ducts) that are not required in the current method, for which the only limitations are that the duct and mean flow vary smoothly with position. This work extends the scope of the eigenvector approach to include acoustic problems previously limited to volumetric or surface-based methods.

Key words: perturbation, Euler, curvilinear, non-orthogonal, eigenvalue, eigenvector

Nomenclature

A_{rl}, B_{rl} (& similar)	Submatrices (defined in equation 31) of eigenvector matrix E_i
c_{ir}, c_{il}, c_{ih}	Complex coefficients of right-running, left-running and high order modes respectively at analysis surface i (see section 5.5)
$\hat{c}_{ir}$ (& similar)	Complex coefficients as c_{ir} but referenced to the mid-point ζ_c of each duct section
$\bar{\bar{c}} = \sqrt{\frac{\gamma\bar{\bar{p}}}{\bar{\bar{\rho}}}}$	Representative speed of sound (m/s)
$\bar{c} = \sqrt{\frac{\bar{p}}{\bar{\rho}}}$	Correction factor to account for the local speed of sound (see text)
D_ξ, D_η	Linear differential operators acting in the ξ and η directions
E_i	Eigenvector matrix at analysis surface i
f'	Representative perturbation variable: $O(f')^n$ means terms where the combined order of perturbation variables is greater than or equal to n
$f = \begin{pmatrix} u_\xi' \\ u_\eta' \\ u_\zeta' \\ p' \end{pmatrix}$ or $\begin{pmatrix} u_\xi' \\ u_\eta' \\ u_\zeta' \\ p' \\ \rho' \end{pmatrix}$	Vector representing the unknown perturbation variables
g_{ij}, g^{ij}, g	Metric tensor, its inverse and its determinant respectively
I_n	Identity matrix of rank n
$k_{\zeta n} = \mathrm{i}\lambda_\mathrm{n}$	Pseudo-axial wavenumber of n$^{\text{th}}$ eigenmode according to the convention $e^{-ik_{\zeta n}\zeta}$
L	Representative lengthscale. In the validation cases $L = 1m$.
m	Circumferential or pseudo-circumferential mode number
$\bar{\bar{p}}$	Representative pressure (Pa)
p	Pressure normalised by $\bar{\bar{p}}$
$\bar{p}$	Time average pressure normalised by $\bar{\bar{p}}$ (aerodynamic scaling)
p'	Perturbation pressure normalised by $\gamma\bar{\bar{p}}$ (acoustic scaling)
r_1, r_2	Complex coefficients of reflected waves (see section 5.5)
s_1, s_2	Matrices used in calculating reflected waves (defined in equ 35)
r_{iw}, r_{ow}	Inner and outer wall radii
R	Outer wall radius (cylindrical) or mean radius (axially extruded duct) normalised by L
t	Time normalised by $L/\bar{\bar{c}}$
$\boldsymbol{u}$	Velocity normalised by $\bar{\bar{c}}$
$\bar{\boldsymbol{u}}, \boldsymbol{u}'$	Time average and perturbation velocity normalised by $\bar{\bar{c}}$
u_ξ, u_η, u_ζ	Components of covariant velocity tensor (that is, coefficients of contravariant basis vectors in (ξ, η, ζ) coordinate system)
u_i, u^i	i^{th} component of covariant and contravariant velocity tensors respectively
$\boldsymbol{x} = (x, y, z)$	Position normalised by L
X_{12}	Transfer matrix between incoming and outgoing modes to the duct section between analysis surfaces 1 and 2

$X_{in}, X_{basis}, X_{out}$	Transfer matrices representing transmission from the end of a duct section to the midpoint, the change of basis at the mid-point, and transmission from the mid-point to the end of a duct section respectively, as defined in section 5.5
γ	Ratio of specific heats
ϵ^{ijk}	Permutation tensor, related to the permutation symbol e^{ljk} by $\epsilon^{ljk} = \frac{1}{\sqrt{g}} e^{ljk}$ (see Appendix A)
λ_n	Eigenvalue of nth eigenmode
(ξ, η, ζ)	Global curvilinear coordinate system
$\hat{\boldsymbol{\xi}}, \hat{\boldsymbol{\eta}}, \hat{\boldsymbol{\zeta}}$	Standard contravariant basis vectors in (ξ, η, ζ) coordinate system
$\bar{\bar{\rho}}$	Representative density (kg/m^3)
ρ	Density normalised by $\bar{\bar{\rho}}$
$\bar{\rho}, \rho'$	Time average and perturbation density normalised by $\bar{\bar{\rho}}$
ω	Angular frequency normalised by $\bar{\bar{c}}/L$
$\zeta_c = \frac{(\zeta_1 + \zeta_2)}{2}$	Midpoint of a duct section between adjacent analysis surfaces $\zeta = \zeta_1$ and $\zeta = \zeta_2$

1. Introductory Remarks

Eigen analysis is widely used in analysis of flow perturbations in *uniform* ducts with *uniform* mean flow, because

1. It offers the engineer a framework with which to 'understand' the problem – to understand the behaviour of each individual eigenmode is, for a wide range of linear engineering problems, to understand the system.
2. It offers an extremely fast prediction route.

Moving from uniform to non-uniform ducts and mean flow, and moving from regular orthogonal coordinate systems to irregular non-orthogonal coordinate systems, greatly reduces the first benefit. The eigenmodes themselves change shape along the duct, so any understanding of how individual modes behave is necessarily limited to that part of the duct for which the modes were calculated.

The tenet of this paper is that the second benefit remains – it will be shown that when the mean flow is non-uniform the computational expense of performing calculations in general curvilinear coordinates is of the same order as that required for more approximate calculations based on conventional orthogonal systems such as cylindrical polars. Consequently this new and more general approach has potential application in a wide variety of fields.

2. State of the Art

Duct propagation methods can be broadly classified as

a) Volumetric, including finite difference, finite volume, finite element and Lagrangian methods.
b) Surface-based, including boundary element methods and derivatives.
c) Semi-analytic, including eigen analysis methods.

Volumetric methods are the most general, capturing general geometry and mean flow profiles, but are the most expensive computationally. Surface-based schemes can handle any smoothly-varying duct geometry but become complex if the mean flow is non-uniform and/or rotational. Semi-analytic schemes can be extremely fast, but can also be difficult to apply in ducts with irregular geometry and/or non-uniform mean flow.

The scope of this paper is limited to semi-analytic eigen analysis methods.

Eigen analysis methods have been used for many years to aid understanding of acoustic propagation in ducts: Tyler and Sofrin's [1] widely referenced work on aeroengine tone noise is based on eigen analysis of uniform annular cylindrical ducts with uniform axial mean flow.

2.1. *Eigen Analysis in Slowly Varying Ducts*

Rienstra [2] combined the eigenvalue approach with a multiple-scales methodology to accommodate annular cylindrical ducts of slowly-varying radius. Peake and Cooper [3] extended the method to elliptical ducts, and Rienstra [4] further extended the method to incorporate slowly varying axial ducts of arbitrary cross-section. This last paper provides a step toward the current method, in that a numerical method was used to calculate eigenmodes at successive analysis planes. The slowly-varying requirement was still needed, however, to simplify the analysis and to allow the boundary conditions to be treated in the same way as a parallel duct – that is, the axial component of the wall normal could be neglected. Astley et al [5] developed a method for eigen-analysis in a uniform cylindrical annular duct with circumferentially varying mean flow and provided a direct comparison with results from an aeroengine-representative inlet.

Rienstra's work was limited to axially aligned ducts. Brambley and Peake [6] adopted a similar approach to accommodate strongly curved slowly varying cylindrical ducts (that is, ducts with circular/annular cross-section where the wall radii vary slowly with distance along the duct centreline). The analysis surfaces were again planar, although in this case the planes were no longer parallel. Restricting analysis to slowly varying cylindrical ducts permitted the same approximation with respect to the walls – namely that they could be treated as normal to the analysis plane.

Both Rienstra and Brambley and Peake considered sound propagation in potential mean flow, which allows the use of a reduced equation set. Cooper and Peake [7] included the effects of mean flow vorticity, and Cooper [8] studied the effect of non-homentropic mean flow in the swirling region downstream of a bladerow and showed a modest effect on the axial wavenumber of acoustic waves, concluding that it can be an important effect close to the cut-on/cut-off boundary.

The conventional paradigm for eigen analysis, exemplified in most of the papers referenced above, is to use a locally accurate approximation to the geometry for which a locally-fitted orthogonal coordinate system can readily be applied, with the duct boundaries approximately or exactly following the coordinate axis normal to the plane.

The current work constitutes a shift away from this paradigm toward the use of a single, global, body-fitted coordinate system. This method is more complex, but brings with it several advantages:

- The slowly-varying limitation in the previous work is removed. Ducts still have to be smooth but duct geometry and mean flow can vary strongly with position.
- The gaps left by previous analyses (for instance strongly curved ducts with arbitrary cross-section) are filled.
- This is achieved within a single framework.
- The coordinate system can be chosen to optimise computational efficiency.

2.2. *Studies Deriving from Analysis of Waveguides*

A second strand of work in this field stems originally from the study of electromagnetics in waveguides. Most of this work is restricted to solutions of the Helmholz equation with zero or uniform mean flow, but some of the same issues are faced in the consideration of non-uniform geometry and/or non-uniform wall impedance. Pagneux et al [9] introduced a multi-modal method for acoustic propagation based on hardwall duct modes for a prescribed geometry of varying area. Various extensions of this method have been made for specific cases: Felix and Pagneux [10], for example, apply the method to bends in three-dimensional ducts of circular cross section with and without an impedance condition at the duct walls. More recent treatments, see for instance Felix et al [11], include a 'supplementary mode' for lined ducts to satisfy the impedance boundary condition at the duct walls without the need to include very large numbers of hardwall modes in the model. Maurel et al [12] have extended the approach in two dimensions to non-uniform ducts using a Jacobian-based transformation.

This last paper [12], using a Jacobian-based transformation in two dimensions, takes a step towards the current work, albeit for a much restricted problem set. In the current method the problem is framed in curvilinear coordinates in three dimensions, and the effects of non-uniform mean flow are included, which greatly expands the range of application to engineering problems of interest. A further departure from the above studies is that the current method is based on a set of modes at each analysis surface that fully obey the local boundary conditions, whereas the above studies are based on a modal series solution to the hardwall

problem in uniform geometry. The current method is a more natural approach and removes one of the sources of error discussed in the above studies (the convergence of the solution series to a true duct solution). The reasons given by Mercier and Maurel [13] for the latter choice are twofold: firstly that it is not proven that a mathematically complete series solution exists in the general case, and secondly that "the notion of adapted transverse functions becomes fuzzy" in the case of continually varying impedance. The first issue is not relevant to the current work, as the problem is first discretised, and the eigenmodes found form a complete basis with respect to the discretised problem. The complete basis set is used in propagation, with due regard to modes that are not well captured numerically, avoiding issues that can arise from mode matching using an incomplete basis. The second reason is logical in the sense that there is relatively little research on the use of non-constant eigenmodes in acoustics. Not all of the outstanding questions can be resolved in a single paper, and it is hoped that the wide applicability of the current method, as demonstrated in this paper, will spur further research in this area.

2.3. *Related Applications of Eigen Analysis*

A number of authors have used eigen analysis to explore the behaviour of acoustic liners in the presence of a boundary layer (see for instance Brambley [14]). This is beyond the scope of the current work: although the methods presented in this paper are amenable for analysis of this type, the computational cost is prohibitive for prediction of acoustic propagation in three-dimensional non-uniform geometries and mean flow, which is the main objective of this paper.

Acoustic eigenvector solutions have been widely used for analysing volumetric computational fluid dynamics (CFD) or computational aeroacoustics (CAA) duct flow solutions and to provide non-reflecting boundary conditions (see for example Wilson, [15, 16], Rienstra and Ovendon [17]). This work included numerical eigenmode calculations in axisymmetric ducts to include the effects of radially non-uniform swirling flow profiles (Kousen, [18], Moinier and Giles, [19]). This field is beyond the scope of the current paper.

3. Outline of Method

The inputs to the EAGCC method are:

1. **A duct** described by a single global body-fitted coordinate system, such as the one shown in figure 1. One of the coordinates (here denoted ζ) has to represent the direction of propagation along the duct and can be considered as a "pseudo-axial" coordinate. It is convenient also to define a "pseudo-radial" coordinate ξ, such that the duct boundaries lie on surfaces of constant ξ, and a "pseudo-circumferential" coordinate (η), as shown in the figure. In principle any smoothly-varying coordinate system can be used, but recommendations for selection and generation of a computationally efficient coordinate system are provided in the discussion at the end of the paper.
2. **A time-averaged flowfield**.
3. **An incoming perturbation** at fixed frequency ω at one or both ends of the duct.

The output of the method is the outgoing perturbation at the ends of the duct: both the transmitted and (optionally) the reflected waves. In addition the complete perturbation field is captured at each analysis surface and can be used to map the flow perturbation within the duct. Although the method is described for a single set of input waves, the most computationally expensive part of the calculation is the derivation of the

eigenvector matrices, described below, and these can be re-used to calculate the response to any other incoming perturbations at the prescribed frequency with little additional expense.

The first step in the analysis proper is the generation of eigensolutions to the linearised flow equations on surfaces of constant ζ. The use of general curvilinear coordinates for the analysis captures the effects of curvature in the coordinate system as well as gradients in mean flow amplitude and direction.

The eigensolutions are classified in terms of direction of information travel. If the mean flow is irrotational and homentropic these eigensolutions represent acoustic, vortical and entropic perturbations as in conventional analysis in cylindrical ducts with uniform mean flow. In cases where the rotational and non-homentropic components of the mean flow are not extreme the eigensolutions can still be classified into these perturbation types, as demonstrated in the validation cases given below.

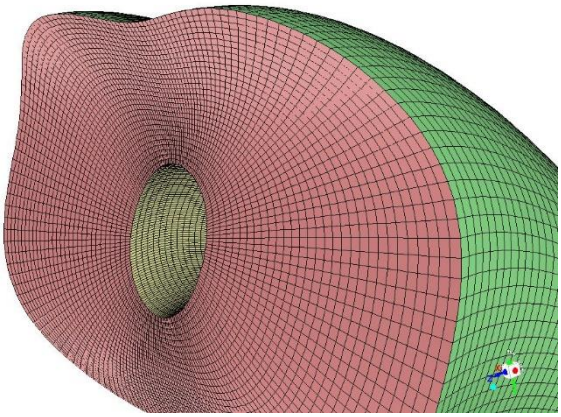

Figure 1. Example of a body-fitted (ξ, η, ζ) coordinate system in a non-uniform duct. The ζ coordinate increases along the length of the duct. The ξ coordinate increases from inner to outer wall and the η coordinate increases in the pseudo-circumferential direction.

The method of propagation along the duct is described in detail in section 5.5. The signal in the vicinity of each analysis surface is described in terms of eigenmode coefficients and the axial variation (amplitude and phase) of each coefficient calculated directly from the related eigenvalue. At the mid-point between analysis surfaces ($\zeta = \zeta_c$) a change of basis matrix is developed to relate the coefficients from one set of eigenmodes to those of the next. This is a first-order discretisation in the sense that the eigenvector basis is approximated as being constant in the vicinity of each analysis surface, but this should not be confused with first-order finite difference schemes: in the latter the phase information has to be captured within the finite difference framework. In the current method the phase information is propagated using the eigenvalues, and hence the method is not subject to the same limitations in terms of mesh points-per-wavelength.

Two forms of axial propagation are considered. A common assumption in previous work is that reflections from geometry and mean flow changes within the duct can be neglected. If the objective of the calculation is a one-way transmission characteristic this can be a good approximation even in the presence of weak-to-moderate non-uniformity in geometry and mean flow, because only secondary reflections (reflections of the reflections) affect the result. This assumption is used in the "one-way sweep" method. Here the signal is filtered at each boundary and only the information travelling in the direction of the sweep (away from the plane of the input signal) is retained.

In the "two-way sweep" method reflections are captured and stored as source values introduced to the succeeding sweep in the opposite direction. Because reflected perturbations can themselves be reflected this

becomes an iterative calculation with successive sweeps in alternate directions. In this type of analysis input signals can be applied at both ends of the duct.

The two types of propagation method are defined mathematically in section 5.5.

The eigenvalue analysis and propagation of perturbations along the duct are based on a description of the flow velocity in terms of standard contravariant basis vectors derived from the coordinate system[1]. A coordinate transformation is needed, therefore, for any vector information input to or output from the method. The mean flow velocity, for example, has to be transformed prior to use, as does the input perturbation velocity at the upstream or downstream end of the duct. Similarly, the output perturbation velocity has to be transformed back into Cartesian or cylindrical polar coordinates in order to be compared with measurements or other calculation methods.

4. Derivation of Equations

The perturbation analysis is based on the linearised Euler equations for a perfect gas. This entails two implied assumptions. The first is the small-perturbation approximation inherent in all linearised analyses. The second is that the perturbations are not subject to viscous effects (either turbulent or laminar), neither to turbulent or radiant heat transfer. These effects are known to be small for free-field propagation over a large number of wavelengths, and a similar relationship can be expected to hold for in-duct propagation.

Note that the mean flow may be viscous, rotational and/or non-homentropic and subject to all of the above effects.

The non-linear Euler equations can be found in standard textbooks on fluid dynamics (see for example Anderson [20] p77-78, together with the equation for the internal energy of a perfect gas on p88). The linearised form of these equations can be written

$$\frac{\partial \boldsymbol{u}'}{\partial t} + \bar{\boldsymbol{u}} \cdot \nabla \boldsymbol{u}' + \boldsymbol{u}' \cdot \nabla \bar{\boldsymbol{u}} + \frac{1}{\bar{\rho}} \nabla \mathrm{p}' - \frac{\rho'}{\gamma \bar{p}^2} \nabla \bar{p} = 0 \qquad \text{(momentum)} \qquad \text{(Eq. 1)}$$

$$\frac{\partial p'}{\partial t} + \bar{\boldsymbol{u}} \cdot \nabla p' + \frac{1}{\gamma} \boldsymbol{u}' \cdot \nabla \bar{p} + \gamma p' \nabla \cdot \bar{\boldsymbol{u}} + \bar{p} \nabla \cdot \boldsymbol{u}' = 0 \qquad \text{(energy/entropy)} \qquad \text{(Eq. 2)}$$

$$\frac{\partial \rho'}{\partial t} + \bar{\boldsymbol{u}} \cdot \nabla \rho' + \boldsymbol{u}' \cdot \nabla \bar{\rho} + \rho' \nabla \cdot \bar{\mathbf{u}} + \bar{\rho} \nabla \cdot \mathbf{u}' = \mathbf{0} \qquad \text{(mass)} \qquad \text{(Eq. 3)}$$

where $\boldsymbol{u}, p, \rho$ represent velocity, pressure and density respectively, γ is the ratio of specific heats and t is time. An overbar represents a time mean (but spatially varying) quantity and an apostrophe a perturbation from that average. Both mean and perturbation quantities are non-dimensionalised using reference values as shown in the Nomenclature section. Attention is drawn to the fact that mean pressure $\bar{p}$ is normalised by the reference pressure $\bar{\bar{p}}$ (aerodynamic scaling), whereas the perturbation p' is normalised by $\gamma\bar{\bar{p}}$ (acoustic scaling) to align the results with standard convention in acoustics.

If the flow mean flow is, or is close to, homentropic the entropy conservation equation can be used to remove the dependency on ρ', leading to

[1]The velocity vector itself is *covariant*, being described in terms of basis vectors which are *contravariant*.

$$\frac{\partial \boldsymbol{u}'}{\partial t} + \overline{\boldsymbol{u}} \cdot \nabla \boldsymbol{u}' + \boldsymbol{u}' \cdot \nabla \overline{\boldsymbol{u}} + \frac{1}{\bar{\rho}} \nabla p' - \frac{p'}{\gamma \bar{\rho}^2 \bar{c}^2} \nabla \bar{p} = 0 \qquad \text{(momentum)} \qquad \text{(Eq. 4)}$$

$$\frac{1}{\bar{c}^2} \frac{\partial \mathrm{p}'}{\partial t} + \frac{\mathrm{p}'}{\bar{c}^2} \nabla \cdot \overline{\boldsymbol{u}} + \overline{\boldsymbol{u}} \cdot \nabla \left(\frac{\mathrm{p}'}{\bar{c}^2} \right) + \bar{\rho} \nabla \cdot \boldsymbol{u}' + \boldsymbol{u}' \cdot \nabla \bar{\rho} = 0 \quad \text{(mass)} \qquad \text{(Eq. 5)}$$

where $\bar{c} = \sqrt{\frac{\bar{p}}{\bar{\rho}}}$ can be viewed as a local correction to the speed of sound $\bar{\bar{c}}$. (Eq. 6)

In tensor form based on contravariant basis vectors, the non-homentropic form of the linearised Euler equations (equations 1 to 3) can be reformulated using the identities in appendix A to give

$$\frac{\partial u_i'}{\partial t} + \frac{1}{2} \frac{\partial}{\partial x^i} \left(g^{jk} \left[u_j' \bar{u}_k + \bar{u}_j u_k' \right] \right) - \epsilon^{ljk} \epsilon^{mnp} g_{il} g_{km} \left[u_j' \frac{\partial \bar{u}_p}{\partial x^n} + \bar{u}_j \frac{\partial u_p'}{\partial x^n} \right] + \frac{1}{\bar{\rho}} \frac{\partial \mathrm{p}'}{\partial x^i} - \frac{\rho'}{\gamma \bar{\rho}^2} \frac{\partial \bar{\mathrm{p}}}{\partial x^i} = 0 \qquad \text{(Eq. 7)}$$

$$\frac{\partial p'}{\partial t} + g^{ij} \bar{u}_j \frac{\partial p'}{\partial x^i} + \frac{1}{\gamma} g^{ij} u_j' \frac{\partial \bar{p}}{\partial x^i} + \frac{\gamma p'}{\sqrt{g}} \frac{\partial}{\partial x^i} \left(\sqrt{g} g^{ij} \bar{u}_j \right) + \frac{\bar{p}}{\sqrt{g}} \frac{\partial}{\partial x^i} \left(\sqrt{g} g^{ij} u_j' \right) = 0 \qquad \text{(Eq. 8)}$$

$$\frac{\partial \rho'}{\partial t} + g^{ij} \bar{u}_j \frac{\partial \rho'}{\partial x^i} + g^{ij} u_j' \frac{\partial \bar{\rho}}{\partial x^i} + \frac{\rho'}{\sqrt{g}} \frac{\partial}{\partial x^i} \left(\sqrt{g} g^{ij} \bar{u}_j \right) + \frac{\bar{\rho}}{\sqrt{g}} \frac{\partial}{\partial x^i} \left(\sqrt{g} g^{ij} u_j' \right) = 0 \qquad \text{(Eq. 9)}$$

where g_{ij} represents the metric tensor of the coordinate system, g^{ij} its inverse and g its determinant. ϵ^{ljk} is the permutation tensor, related to the permutation symbol e^{ljk} by

$\epsilon^{ljk} = \frac{1}{\sqrt{g}} e^{ljk}$ (see Appendix A). (Eq. 10)

The homentropic form of the equations (equations 4 and 5) can be similarly reformulated to give

$$\frac{\partial u_i'}{\partial t} + \frac{1}{2} \frac{\partial}{\partial x^i} \left(g^{jk} \left[u_j' \bar{u}_k + \bar{u}_j u_k' \right] \right) - \epsilon^{ljk} \epsilon^{mnp} g_{il} g_{km} \left[u_j' \frac{\partial \bar{u}_p}{\partial x^n} + \bar{u}_j \frac{\partial u_p'}{\partial x^n} \right] + \frac{1}{\bar{\rho}} \frac{\partial \mathrm{p}'}{\partial x^i} - \frac{p'}{\gamma \bar{\rho}^2 \bar{c}^2} \frac{\partial \bar{\mathrm{p}}}{\partial x^i} = 0 \qquad \text{(Eq. 11)}$$

$$\frac{1}{\bar{c}^2} \frac{\partial \mathrm{p}'}{\partial t} + \frac{p'}{\sqrt{g} \bar{c}^2} \frac{\partial}{\partial x^i} \left(\sqrt{g} g^{ij} \bar{u}_j \right) + g^{ij} \bar{u}_j \frac{\partial}{\partial x^i} \left(\frac{p'}{\bar{c}^2} \right) + \frac{\bar{\rho}}{\sqrt{g}} \frac{\partial}{\partial x^i} \left(\sqrt{g} g^{ij} u_j' \right) + g^{ij} u_j' \frac{\partial \bar{\rho}}{\partial x^i} = 0 \qquad \text{(Eq. 12)}$$

4.1. *Conventional Eigen Analysis: Uniform Cylindrical Duct Geometry and Uniform Axial Mean Flow in Cylindrical polar coordinates*

This section provides a brief outline of the conventional analysis method for uniform geometry and flow as a template for the description of the current method in the section following. For this restricted case the matrices derived are equivalent to those provided by Kousen [18]).

In uniform axial flow $\bar{\rho}, \bar{p}$ and $\bar{c}^2$ are all constant and (with appropriate choice of reference parameters) take the value of unity.

$\overline{\boldsymbol{u}} = \bar{U} \hat{\boldsymbol{z}}$ where $\bar{U}$ is also constant. (Eq. 13)

The mean flow in this case is homentropic and so the second form of the equations (equations 4 and 5) can be used and reduce to

$$\frac{\partial \boldsymbol{u}'}{\partial t} + \overline{U}\frac{\partial \boldsymbol{u}'}{\partial z} + \nabla p' = 0 \qquad \text{(Eq. 14)}$$

$$\frac{\partial \mathrm{p}'}{\partial t} + \overline{U}\frac{\partial \boldsymbol{p}'}{\partial z} + \nabla \cdot \boldsymbol{u}' = 0 \qquad \text{(Eq. 15)}$$

Taking a Fourier transform in time,

$$\frac{\partial \mathrm{p}}{\partial t} = \frac{\partial \mathrm{p}'}{\partial t} \rightarrow i\omega\tilde{p} \quad \text{(and similar for the velocity components)} \qquad \text{(Eq. 16)}$$

these equations can be re-written in matrix form

$$A\frac{\partial \tilde{f}}{\partial z} = B\tilde{f} \qquad \text{(Eq. 17)}$$

where

$$\tilde{f} = \begin{pmatrix} \tilde{u}_r \\ \tilde{u}_\theta \\ \tilde{u}_z \\ \tilde{p} \end{pmatrix} \qquad \text{(Eq. 18)}$$

$$A = \begin{pmatrix} \overline{U} & 0 & 0 & 0 \\ 0 & \overline{U} & 0 & 0 \\ 0 & 0 & \overline{U} & 1 \\ 0 & 0 & 1 & \overline{U} \end{pmatrix} \qquad \text{(Eq. 19)}$$

$$B = \begin{pmatrix} -i\omega & 0 & 0 & -D_r \\ 0 & -i\omega & 0 & -D_\theta \\ 0 & 0 & -i\omega & 0 \\ -\frac{1}{r} - D_r & -D_\theta & 0 & -i\omega \end{pmatrix} \qquad \text{(Eq. 20)}$$

where $D_r$and D_θ are linear partial derivative operators.

If each of the perturbation parameters is represented on an $n_r \times n_\theta$ orthogonal cylindrical polar mesh then $D_r$and D_θ become partial derivative matrices which can be pre-calculated to any desired order of accuracy. Alternatively a spectral definition may be used in the circumferential direction in which case

$$D_\theta \rightarrow -im \qquad \text{(Eq. 21)}$$

In either case A and B can be calculated explicitly and (generalised) eigen solutions found from equation 17 along with boundary conditions

$u_r = 0$ on the inner and outer walls. (Eq. 22)

4.1.1.*Eigen Analysis in a General Curvilinear Coordinate System*

Consider now a curvilinear coordinate system (ξ, η, ζ) as illustrated in figure 1. This coordinate system can be of any type, but the form illustrated with one variable acting as a pseudo-radial and one as a pseudo-circumferential coordinate is often convenient for duct (cylindrical or annular) calculations as the boundary conditions are easier to apply if the boundaries lie on a surface with one coordinate constant. It also allows for a pseudo-spectral solution in the η coordinate, as shown in the validation examples given later.

In analogy to the uniform flow case above, the target is to rewrite the flow equations in the form

$$A\frac{\partial \tilde{f}}{\partial \zeta} = B\tilde{f} \qquad \text{(Eq. 23)}$$

where now the velocity components are not physical components, but represent coefficients with respect to standard contravariant basis vectors for the particular coordinate system under consideration. In the discrete case each velocity component is described over an $n_\xi \times n_\eta$ mesh, as is the pressure, where n_ξ and n_η represent the number of fixed points if a spatial scheme is used, or harmonic coefficients if a spectral scheme is used.

To illustrate this process, take the term $-\bar{\rho}\nabla \cdot \mathbf{u}'$ from the mass conservation equation, which relates to the term $-\frac{\bar{\rho}}{\sqrt{g}}\frac{\partial}{\partial x^i}\left(\sqrt{g}g^{ij}u_j'\right)$ in equations 9 and 12.

This term can be expanded to

$$-\frac{\bar{\rho}}{\sqrt{g}}\frac{\partial \sqrt{g}g^{\xi\xi}}{\partial \xi}u_\xi' - \frac{\bar{\rho}}{\sqrt{g}}\frac{\partial \sqrt{g}g^{\xi\eta}}{\partial \xi}u_\eta' - \frac{\bar{\rho}}{\sqrt{g}}\frac{\partial \sqrt{g}g^{\xi\zeta}}{\partial \xi}u_\zeta' - \frac{\bar{\rho}}{\sqrt{g}}\frac{\partial \sqrt{g}g^{\eta\xi}}{\partial \eta}u_\xi' - \frac{\bar{\rho}}{\sqrt{g}}\frac{\partial \sqrt{g}g^{\eta\eta}}{\partial \eta}u_\eta'$$

$$-\frac{\bar{\rho}}{\sqrt{g}}\frac{\partial \sqrt{g}g^{\eta\zeta}}{\partial \eta}u_\zeta' - \frac{\bar{\rho}}{\sqrt{g}}\frac{\partial \sqrt{g}g^{\zeta\xi}}{\partial \zeta}u_\xi' - \frac{\bar{\rho}}{\sqrt{g}}\frac{\partial \sqrt{g}g^{\zeta\eta}}{\partial \zeta}u_\eta' - \frac{\bar{\rho}}{\sqrt{g}}\frac{\partial \sqrt{g}g^{\zeta\zeta}}{\partial \zeta}u_\zeta'$$

$$-\bar{\rho}g^{\xi\xi}\left(D_\xi u_\xi'\right) - \bar{\rho}g^{\xi\eta}\left(D_\xi u_\eta'\right) - \bar{\rho}g^{\xi\zeta}\left(D_\xi u_\zeta'\right) - \bar{\rho}g^{\eta\xi}\left(D_\eta u_\xi'\right) - \bar{\rho}g^{\eta\eta}\left(D_\eta u_\eta'\right)$$

$$-\bar{\rho}g^{\eta\zeta}\left(D_\eta u_\zeta'\right) - \bar{\rho}g^{\zeta\xi}\frac{\partial u_\xi'}{\partial \zeta} - \bar{\rho}g^{\zeta\eta}\frac{\partial u_\eta'}{\partial \zeta} - \bar{\rho}g^{\zeta\zeta}\frac{\partial u_\zeta'}{\partial \zeta} \qquad \text{(Eq. 24)}$$

where (as in the conventional analysis above), D_ξ and D_η are linear partial derivative operators that can be represented as derivative matrices for the discrete problem.

The last three terms contain a ζ-derivative of a perturbation variable and hence contribute to matrix A. The other terms all contribute to matrix B.

It can be seen that the formulation in general curvilinear coordinates is complex, containing terms related to the metric tensor as well as the flow variables themselves. For this reason the reformulation of the flow equations into matrix form is better done (and in this work was done) symbolically.

4.2. *Boundary Conditions*

If, as described above, a coordinate system is adopted in which the duct walls are represented by holding one of the coordinates (ξ) constant, then by definition the contravariant basis vector $\hat{\boldsymbol{\xi}}$ is normal to the wall.

Thus the zero flow hardwall boundary condition can be written

$$\hat{\boldsymbol{\xi}} \cdot \boldsymbol{u} = 0 \qquad \text{(Eq. 25)}$$

Or, in tensor form

$$g^{1j} u_j = 0 \qquad \text{(Eq. 26)}$$

5. Implementation

5.1. *Calculation of the Jacobian and Metric Tensor*

The Jacobian and the metric tensor can be pre-calculated directly from the definition of the calculation mesh. This can, however, introduce errors if the calculation mesh is insufficiently fine. In order to eliminate this concern in the current work, a finer (ξ, η, ζ) mesh was generated, and the Jacobian and metric tensor calculated using a linear partial differential operator in each direction similar to that used for the perturbation variables (described in the following section).

5.2. *Differentiation in Directions other than the Direction of Propagation*

The equations derived in the above section include derivative operators D_ξ and D_η in directions other than the direction of propagation.

In the ξ direction this derivative was represented by a matrix in which the ith row represents the coefficients needed to provide a fourth order polynomial approximation of the derivative at point i using a 5 point stencil.

In the validation examples below, a pseudo-spectral solution was sought in the η direction, for which the first order differentiation matrix D_η is a diagonal matrix $\begin{bmatrix} -im_1 & \cdots & 0 \\ \vdots & \ddots & \vdots \\ 0 & \cdots & -im_n \end{bmatrix}$ where m_k is the k^{th} circumferential order in η.

In the equations above these matrices have to be expanded to operate on full $(n_\xi \times n_\eta)$ vectors. This is done independently in the two directions – that is D_ξ is expanded to operate along each line of constant η and vice-versa.

The differentiation matrices obtained were used in two ways: for predetermined variables including the time mean variables and metric tensor they were applied directly in the pre-processing step as operators acting on these variables. For the linear perturbation variables, which are initially unknown, they are applied directly in matrix form as submatrices in equation 23.

5.3. *Implementation of Boundary Conditions*

There is some freedom as to how to implement the boundary conditions. Maldonado et al [21], working with uniform annular ducts, found that best results were obtained by preserving the normal pressure gradient in the equation set. Accordingly, the boundary conditions in this method were implemented by replacing the rows in matrices A and B in equation 23 related to the continuity equation at the inner and outer wall with terms representing equation 26. Without removing rows from the matrix this leads in the eigensolution to a number of eigenvectors with infinite (or extremely large) eigenvalues. These eigenvectors do not represent feasible solutions and can be ignored in the propagation calculations.

In this analysis modal coefficients are obtained by inverting the eigenvector matrix, and in some cases the presence of these inadmissible eigenvectors caused instabilities in the solution. In these cases more robust results were obtained by replacing these vectors with an arbitrary orthogonal set spanning the space of inadmissible vectors – this makes no difference to the overall solution as these vectors are not in any case used in the propagation calculations.

5.4. *Eigenvectors and Eigenvalues*

Having derived equation 23, eigenvectors and eigenvalues were obtained using a standard eigensolver[2].

The propagation method (see next section) requires the eigenmodes to be classified into three categories:

- Right-running (acoustic and vortical or acoustic only depending on the direction of the mean flow)
- Left-running (acoustic and vortical or acoustic only depending on the direction of the mean flow)
- High order (acoustic or vortical, not well captured in the discretised system)

It is accepted that the higher order perturbations with transverse wavelengths up to a small multiple of the mesh spacing will not be correctly captured in the eigensolution process (and neither in the validating CFD calculation). Most of these eigenmodes are strongly cut-off, and hence are of little practical interest. These modes were classified as 'high order' based simply on the amplitude of the eigenvalue. Due to the numerical discretisation some high order modes can also be in the wavenumber range of interest. Moinier and Giles [19] introduced a fourth order smoothing term to ensure that high order spurious modes had eigenvalues away from the region of interest, but for the validation cases shown here it was found not to be necessary: the high order modes contained little energy and did not contaminate the solutions (see section 6.1 for further discussion).

In the validation cases presented in this paper it was possible to accurately classify the remaining eigenvectors by comparison of the eigenvalue (or wavenumber $k_{\zeta n}$) set with known solutions for uniform mean flow in cylindrical ducts, as illustrated in Figure 2, Figure 6 and Figure 15. In all cases there was a clear separation of the eigenvalues between cut-on and cut-off modes and upstream and downstream-travelling modes, and classification was performed using simple linear programming. In validation case 4 below, with axially non-uniform geometry and mean flow, the classification was checked manually at each analysis surface along the duct and the coefficients of the linear programming adjusted where necessary.

It is recognised that this simple classification method will not be appropriate in more complex cases with very strongly non-uniform or swirling flow or regions of reversed flow and further work is required.

Division into acoustic and vortical modes was based on the pressure content of the mode calculated as the root mean square [normalised] pressure amplitude divided by the root mean square [normalised] velocity amplitude. It is noted, however, that an accurate division between downstream acoustic and downstream vortical modes is not required for the EAGCC method.

5.5. *Propagation along the Duct*

Given the classification of the eigenmodes as described in the previous section the eigenvalue matrix at any analysis surface 1, defined by $\zeta = \zeta_1$, can be ordered $(E_{1r}\ E_{1l}\ E_{1h})$ representing the right-running (r), left-running (l) and high order (h) modes respectively. No distinction beyond this is necessary: acoustic, vortical and in the more general case entropy modes are all included in the calculations. The complex coefficients of

[2]the eig function in MATLAB version R2015a

each mode on the surface are labelled $c_1 = \begin{pmatrix} c_{1r} \\ c_{1l} \\ c_{1h} \end{pmatrix}$. Right-running waves are defined as those propagating from surface 1 to an adjacent analysis surface 2 ($\zeta = \zeta_2$) with eigenvectors and modal coefficients similarly ordered.

5.5.1. *Local transfer matrix*

This section describes the derivation of a transfer matrix X_{12} from the modal coefficients $\begin{pmatrix} c_{1r} \\ c_{2l} \end{pmatrix}$ representing information travelling into the duct section $\zeta_1 < \zeta < \zeta_2$, and the modal coefficients $\begin{pmatrix} c_{2r} \\ c_{1l} \end{pmatrix}$ representing information travelling out of the duct section, such that

$$\begin{pmatrix} c_{2r} \\ c_{1l} \end{pmatrix} = X_{12} \begin{pmatrix} c_{1r} \\ c_{2l} \end{pmatrix} \quad \text{(Eq. 27)}$$

The higher order modes, although not appearing in the input and output vectors, play an important role in the derivation of the transfer matrix X_{12}, as will be seen later.

This transfer matrix X_{12} is calculated in three parts:

$$X_{12} = X_{out} X_{basis} X_{in} \quad \text{(Eq. 28)}$$

where X_{in} represents convection of inward-travelling information from surfaces 1 and 2 to a central surface at $\zeta_c = \frac{(\zeta_1 + \zeta_2)}{2}$. X_{basis} is the change of basis at the central plane: reflections in the duct section are accounted for at this point. X_{out} represents convection of outward-travelling information from the central surface back to surfaces 1 and 2.

Let $\tilde{c}_{1r}$ and $\tilde{c}_{1u}$ define the right- and left-running eigenvectors at the central surface defined according to the eigenmode basis calculated at surface 1, and $\tilde{c}_{2r}$ and $\tilde{c}_{2u}$ according to the basis at surface 2. With this definition,

$$\begin{pmatrix} \tilde{c}_{1r} \\ \tilde{c}_{2l} \end{pmatrix} = X_{in} \begin{pmatrix} c_{1r} \\ c_{2l} \end{pmatrix}, \quad \begin{pmatrix} \tilde{c}_{2r} \\ \tilde{c}_{1l} \end{pmatrix} = X_{basis} \begin{pmatrix} \tilde{c}_{1r} \\ \tilde{c}_{2l} \end{pmatrix} \quad \text{and} \quad \begin{pmatrix} c_{2r} \\ c_{1l} \end{pmatrix} = X_{out} \begin{pmatrix} \tilde{c}_{2r} \\ \tilde{c}_{1l} \end{pmatrix}. \quad \text{(Eq. 29)}$$

The propagation matrices X_{in} and X_{out} are diagonal matrices based on the eigenvalues at surfaces 1 and 2 according to the direction of travel:

$$X_{in} = \begin{pmatrix} X_{1r} & 0 \\ 0 & X_{2l} \end{pmatrix}, \quad X_{out} = \begin{pmatrix} X_{2r} & 0 \\ 0 & X_{1l} \end{pmatrix} \quad \text{(Eq. 30)}$$

where X_{1r} is a diagonal matrix of propagation coefficients $e^{iv_{1rj}\frac{(\zeta_c - \zeta_1)}{2}}$ where v_{1rj} is the eigenvalue associated with the jth right-running eigenmode at plane 1, and the remaining matrices X_{1l}, X_{2r} and X_{2l} are defined in an equivalent manner.

It remains to derive the central transfer matrix X_{basis}.

The physical effects of mode scattering and reflection due to mean flow and geometry changes are captured mathematically by the change of basis from E_1 to E_2. The change of basis matrices in each direction can be decomposed in the same way as the eigenmode matrices:

$$E_2^{-1}E_1 = \begin{pmatrix} A_{rr} & A_{rl} & A_{rh} \\ A_{lr} & A_{ll} & A_{lh} \\ A_{hr} & A_{hl} & A_{hh} \end{pmatrix}, \qquad E_1^{-1}E_2 = \begin{pmatrix} B_{rr} & B_{rl} & B_{rh} \\ B_{lr} & B_{ll} & B_{lh} \\ B_{hr} & B_{hl} & B_{hh} \end{pmatrix}. \qquad \text{(Eq. 31)}$$

The inclusion of the high order terms makes the basis complete. It is important to include the effects of information scattering from the captured modes to the high order modes – it is not sufficient in general to apply a simple mode-matching method between the well captured modes. At the same time it is assumed that the high order modes are highly evanescent: information scattered to these modes should be neglected: backscatter from the high order modes to the captured modes is unwarranted and can cause instabilities in the model. These conflicting requirements can be reconciled by carefully respecting the direction of information flow.

The unsteady flow at the central plane can, in the E_1 basis, be decomposed into downstream modes $\tilde{c}_{1r}$ propagating from upstream, downstream modes r_1 representing reflection of information coming from downstream, and upstream modes $\tilde{c}_{1l}$ propagating from downstream. A similar decomposition can be performed in the E_2 basis. Respecting the direction of information flow, the appropriate relations to model this situation are

$$\tilde{c}_{2r} = A_{rr}(\tilde{c}_{1r} + r_1), \quad \tilde{c}_{1l} = B_{ll}(\tilde{c}_{2l} + r_2), \qquad \text{(Eq. 32)}$$

with the following compatibility conditions

$$r_1 + B_{rl}(\tilde{c}_{2l} + r_2) = 0, \quad r_2 + A_{lr}(\tilde{c}_{1r} + r_1) = 0 \qquad \text{(Eq. 33)}$$

where in each case back-scattering from high order modes is neglected.

Combining the last two equations gives

$$(I - B_{rl}A_{lr})r_1 + B_{rl}(\tilde{c}_{u2} - A_{lr}\tilde{c}_{r1}) = 0. \qquad \text{(Eq. 34)}$$

The term $B_{rl}A_{lr}$ relates to 'double reflections': for a smooth duct (and sufficient discretisation along it) this term will be small, ensuring that $(I - B_{rl}A_{lr})$ is of full rank, giving

$$r_1 = -s_1 B_{rl}(\tilde{c}_{2l} - A_{lr}\tilde{c}_{1r}) \text{ where } s_1 = (I - B_{rl}A_{lr})^{-1} \text{ and similarly}$$
$$r_2 = -s_2 A_{lr}(\tilde{c}_{1r} - B_{rl}\tilde{c}_{2l}) \text{ where } s_2 = (I - A_{lr}B_{rl})^{-1}. \qquad \text{(Eq. 35)}$$

Substituting these into the equations for $\tilde{c}_{2r}$ and $\tilde{c}_{1l}$ gives the transfer matrix in the required form:

$$\begin{pmatrix} \tilde{c}_{2r} \\ \tilde{c}_{1l} \end{pmatrix} = X_{basis} \begin{pmatrix} \tilde{c}_{1r} \\ \tilde{c}_{2l} \end{pmatrix}, \text{ where} \qquad \text{(Eq. 36)}$$

$$X_{basis} = \begin{pmatrix} A_{rr}(I + s_1 B_{rl} A_{lr}) & -A_{rr} s_1 B_{rl} \\ -B_{ll} s_2 A_{lr} & B_{ll}(I + s_2 A_{lr} B_{rl}) \end{pmatrix} \quad \text{(Eq. 37)}$$

These equations can be compared with those of Felix and Pagneux [22], but note the inclusion in the current work of the higher order terms in calculating the matrices.

5.5.2. *"One-way Sweep" Method*

If reflections due to changing duct geometry and mean flow can be neglected, the local transfer matrix in the previous section can be simplified. Taking for example the case where only right-running waves are retained the local transfer matrix becomes

$$X_{21} = X_{out} X_{basis} X_{in} = X_{2r}\, A_{rr}(I + s_1 B_{rl} A_{lr}) X_{1r} \quad \text{(Eq. 38)}$$

where the order of the subscripts in X_{21} has been reversed in cognisance of the fact that in this restricted case it does indeed represent a transfer matrix from surface 1 to surface 2.

Having determined this transfer matrix as described in the previous section the solution at any point along the duct can be obtained in trivial fashion by stepping along the duct:

$$c_{\mathrm{n}r} = X_{n,n-1} X_{n-1,n-2} \ldots X_{32} X_{21} c_{1r} \quad \text{(Eq. 39)}$$

5.5.1. *"Two-way Sweep" Iterative Method*

If reflections along the duct cannot be ignored then the full transfer matrix X_{12} is applied. In this work the solution was obtained using an iterative method. In the first "sweep" all of the left-running modal amplitudes are set to zero, and the solution is stepped from left-to-right, giving identical results to the "one-way sweep" method as defined in the previous section, except that at each interface the coefficients $c_{\mathrm{n}l}$ of the reflected left-running waves are calculated alongside those of the right-running waves. In the second "sweep" the calculation is stepped from right to left, starting with any input wave at the right-hand end of the duct and setting the right-running modal amplitudes to zero. At each interface the reflected waves, defined by the coefficients $c_{\mathrm{n}l}$, are subtracted from the solution prior to propagating through the next duct section. This time the coefficients $c_{\mathrm{n}r}$ of the reflected right-running waves are calculated and stored. This "two-way sweep" is performed iteratively to achieve a converged solution where the calculated coefficients do not change significantly between iterations. At convergence all of the local transfer matrices $\mathrm{X}_{\mathrm{n}-1,\mathrm{n}}$ are satisfied and hence the calculated solution includes the effects of (multiple) reflections.

6. Validation Cases

Five validation cases are presented in this section, as summarised in the table below.

Case	Geometry	Mean Flow	Main Target for Validation
1	Uniform axisymmetric	Uniform	Accuracy of eigenvalue calculation
2	Axially uniform but non-axisymmetric	Uniform	Effect of wall shape on eigen analysis
3	Axially uniform but non-axisymmetric	Axially uniform but non-axisymmetric	Effect of mean flow on eigen analysis

4	Non-Uniform	Non-Uniform	Effect of non-uniformity on acoustic propagation
5	Axially non-uniform but axisymmetric	Zero	Ability of two-way sweep method to capture reflections along a strongly-varying duct.

Table 1. Summary of the validation cases presented in sections 6.1-6.5.

All of these cases are at low to moderate non-dimensional frequency. Wilson [23] provides an additional validation case for aeroengine inlet at aeroengine-representative non-dimensional frequencies.

6.1. *Validation Case 1: Uniform Axisymmetric Annular duct and Uniform Axial Mean Flow*

This case has a well-known analytic solution in the form of Bessel-Fourier harmonics (see, for example, Rienstra and Hirschberg [24]).

The inner and outer radii of the duct were 0.1m and 0.432m respectively. The mean flow was axial in the positive ζ direction with Mach number 0.5. The mean flow is homentropic and thus the simplified method (based on equations 4 and 5) was applied.

The numerical solution was obtained using a uniform radial mesh with 21 points and a pseudo-spectral mesh in the theta dimension covering circumferential harmonics *m* from -17 to +17. In this case the mesh is, of course, orthogonal and the results could have been obtained with conventional eigen-analysis in cylindrical polar coordinates. The signal frequency ω was set such that

$$\omega R = 2.049 \quad \text{(in dimensional terms approximately 250Hz)} \qquad \text{(Eq. 40)}$$

In this test case, where the (ξ, η, ζ) coordinate system matches exactly the cylindrical polar (r, θ, z) coordinate system, the eigenvalues λ_n can be plotted (see figure 2) as axial wavenumbers $k_{\zeta n}$ multiplied by the outer wall radius *R*. Theoretical wavenumbers are also shown for the upstream travelling modes closest to cut-on. The calculated and theoretical wavenumbers follow the same pattern, and the classification of the calculated wavenumbers into acoustic and vortical modes, as shown in the figure, is based on the known behaviour of the theoretical results.

The higher harmonics (with imaginary part of $k_{\zeta n}R$ above about 15) are not expected to be captured correctly and wander somewhat from the vertical line seen at lower order. The zoomed graph on the right shows that the eigenvalues of the lower acoustic modes are all captured accurately, but also shows a small number of spurious modes at eigenvalues without an equivalent Bessel-Fourier mode.

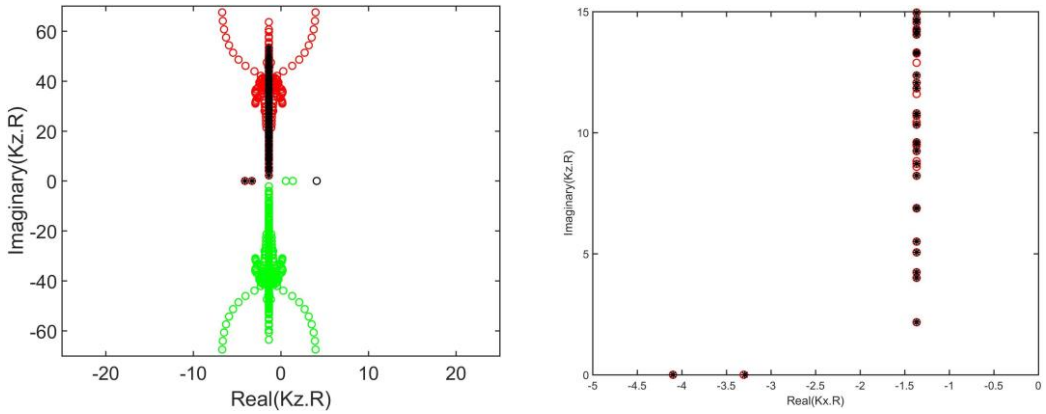

Figure 2. Axial wavenumbers divided into upstream acoustic modes (red circles), downstream acoustic modes (green circles) and vortical modes (black circles). Also shown are theoretical wavenumbers for the upstream-travelling acoustic modes closest to cut-on (black stars). The right hand plot gives an expanded view of the upstream-travelling modes of interest.

The spurious modes all contain high order oscillations in the ξ direction, and can be moved out of this range using a small amount of fourth order smoothing as described by Moinier and Giles [19].

Table 2 shows wavenumbers for sample low order modes (m=4) and high order modes (m=17) with and without smoothing, compared to a value calculated directly from the Bessel-Fourier mode. The level of smoothing applied was the minimum required to shift the spurious modes out of the region of interest ($\mathrm{Im}(k_\zeta R) < 15$).

Circumferential Harmonic (m)	Radial Harmonic	Bessel Fourier $k_z R$	Eigensolution $k_z R$	Eigensolution with smoothing $k_z R$
4	1	-1.37 + 4.00i	-1.37 + 4.00i	-1.37 + 4.00i
4	2	-1.37 + 8.72i	-1.37 + 8.71i	-1.37 + 8.72i
4	3	-1.37 + 12.38i	-1.37 + 12.36i	-1.37 + 12.43i
4	4	-1.37 + 16.13i	-1.37 + 16.13i	-1.39 + 16.34i
17	1	-1.37 + 20.68i	-1.37 + 20.67i	-1.37 + 20.61i
17	2	-1.37 + 26.72i	-1.37 + 26.78i	-1.39 + 26.81i
17	3	-1.37 + 31.46i	-1.37 + 31.35i	-1.42 + 31.91i
17	4	-1.37 + 35.82i	-0.71 + 35.16i	-1.43 + 37.04i

Table 2. Wavenumbers for sample modes compared with wavenumbers for the equivalent Bessel-Fourier Mode

Without smoothing the eigensolution is accurate for the low order modes. The eigenvalues of the cut-on modes are not shown, but are similarly accurate. The eigensolution is somewhat in error for the highest mode shown (fourth radial harmonic at m=17), but that is outside the region of interest ($\mathrm{Im}(k_\zeta R) < 15$). With

smoothing there is a modest error in the higher radial harmonics at m=4 and larger but acceptable errors at m=17.

Validation cases 2 and 3 below were calculated with and without smoothing, with no appreciable difference in the results: although the spurious modes are present, they are either highly cut-off or contain too little energy to contaminate the results. Accordingly, the remaining results in this paper are presented without smoothing.

Figure 3 below shows sample radial pressure profiles for three specific modes compared with analytic Bessel-Fourier modes. As with the eigenvalues the agreement at low orders is very good, but at the highest order (radial harmonic 4 at *m*=17) the eigensolution starts to drift. Note, however, that this mode is strongly cut-off ($\mathrm{Im}(k_\zeta R) \approx 35$).

The results shown in this section demonstrate that the current method, with the given radial and pseudo-spectral definition, accurately captures the modes of interest in this case (both the cut-on modes and the slightly-to-moderately cut-off modes).

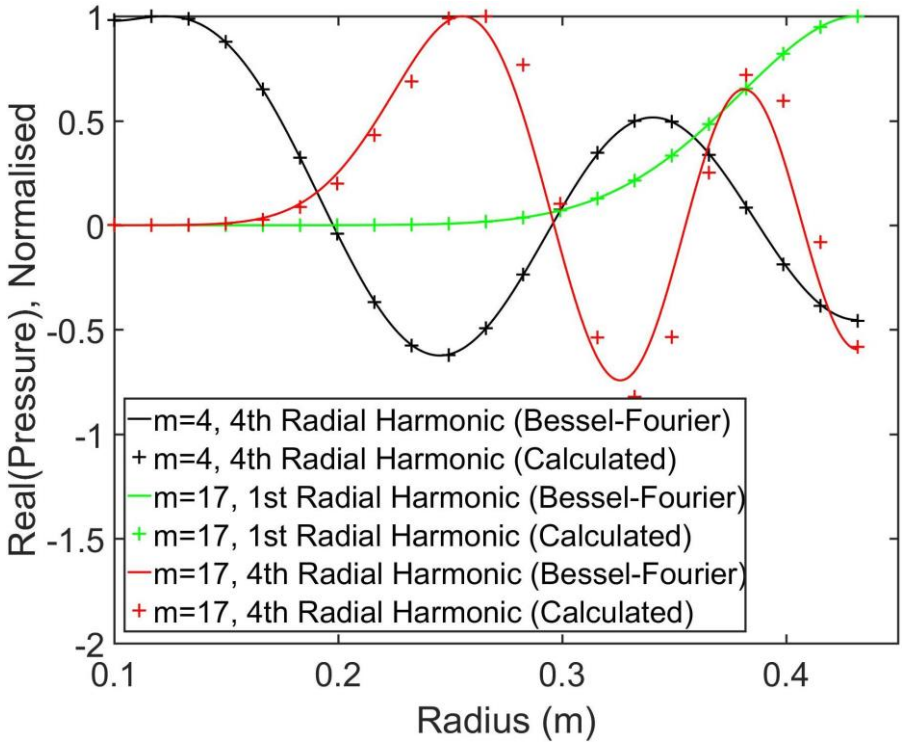

Figure 3. Radial pressure profile for a selection of circumferential (m) and radial harmonics compared with analytic Bessel-Fourier modes.

6.2. *Validation Case 2: Extruded Non-Axisymmetric Annular duct and Uniform Mean Flow*

6.2.1. *Geometry, Mean Flow and Perturbation Source*

The geometry for this test case is an axially extruded duct with cross-section as shown in figure 4.

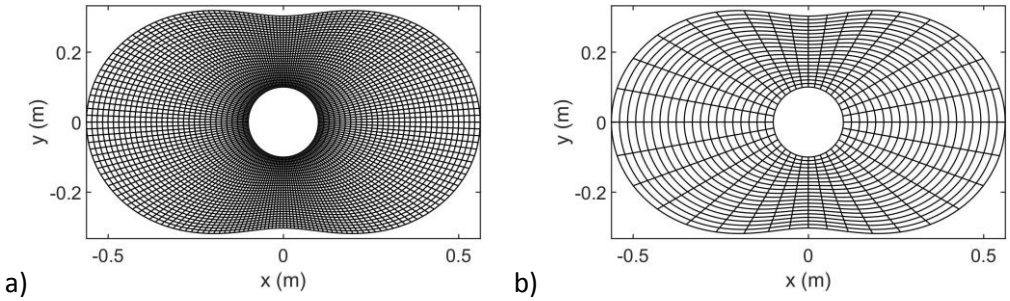

Figure 4. Cross-Section of duct in validation case 2, showing a) the mesh used in validation CFD calculation, b) the mesh used in EAGCC method (lines of constant ξ and η).

The test section was approximately 1 radius long.

The inner and outer wall positions were defined in cylindrical polar notation as:

$$r_{iw} = 0.1 \text{ constant (cylindrical)} \qquad \text{(Eq. 41)}$$

$$r_{ow} = 0.432(1 + 0.3\cos 2\theta) \qquad \text{(Eq. 42)}$$

The mean flow was axial in the positive ζ direction with Mach number 0.5.

A periodic pressure pulse of low amplitude was applied at $\omega R = 2.049$ over a fixed sector at the downstream (outlet) end of the duct as shown in figure 5. The semi-analytic and validating CFD calculations were then applied to predict the flow profile at the upstream (inlet) end of the test section.

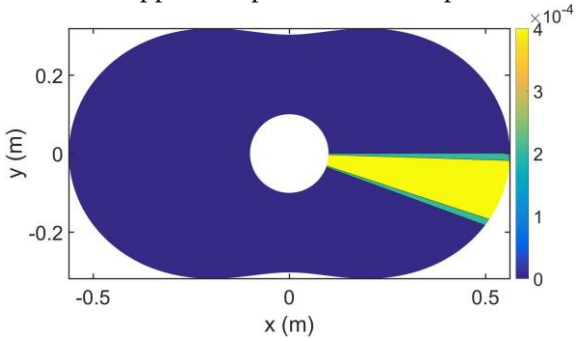

Figure 5. Input pressure pulse region (yellow). The input region is sharp-edged – the region in green represents interpolation between cell-centres.

6.2.2. *Validation Calculation (CFD)*

There is no analytic solution for this case, and validation is against a commercial CFD code[3] run in inviscid non-linear mode using a perturbation amplitude of 1% of the mean pressure. A 31x180x44 (radial x circumferential x axial) hexagonal mesh was used in the test section (figure 4) with a timestep equivalent to one fiftieth of a cycle. The cut-on acoustic modes (see below) have at most a single lobe circumferentially, and hence this definition is sufficient to propagate not only the cut-on acoustic modes but also many of the cut-off modes to the upstream plane without appreciable dissipation error.

[3]ANSYS FLUENT version R17.0

The CFD mesh included also an upstream extension to damp boundary reflections. This extension contained 36 additional axial planes, with the axial distance between the planes increasing geometrically upstream with ratio 1.2.

6.2.3. *Semi-analytic Method*

The mean flow in this case is again homentropic and the simplified method (based on equations 4 and 5) was applied.

The mesh used as a basis for the eigenvalue calculation is shown in Figure 4. The η coordinate corresponds directly to the θ coordinate. The ξ coordinate is linearly scaled from r_{iw} on the inner wall to r_{ow} on the outer wall. Note that the mesh is no longer orthogonal, and also that the outer wall is no longer orthogonal to the pseudo-radial local coordinate axis.

The mean geometry and mean flow parameters for this case (mean inner and outer wall radii and mean axial Mn) were chosen to match validation case 1. Accordingly the same definition was used in the radial and circumferential directions; 21 points equispaced in the radial direction and circumferential modes m from -17 to +17.

6.2.4. *Eigenvalues and Modeshapes*

Figure 6 shows the eigenvalues plotted as wavenumber times the mean outer wall radius for ease of comparison with those predicted for a circular annular duct of the same mean radius shown in figure 2. Given the broad similarity of the eigenvalues to the annular duct solution, it was assumed that the mode type and direction of propagation of each mode followed the same pattern (as illustrated in the figure).

It is noticeable that the lower order wavenumbers shown (that is, wavenumbers the imaginary part of which are close to zero) are similar in pattern to those obtained for the annular duct, but with reduced imaginary part, indicating less cut-off behaviour; indeed the lowest cut-off mode has here become cut-on.

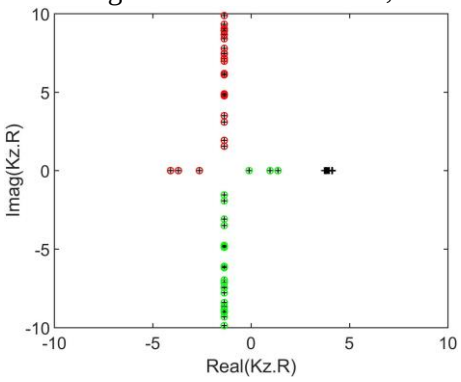

Figure 6. ζ-wavenumber times mean outer wall radius, classified as upstream-travelling acoustic (red), downstream-travelling acoustic (green) and vortical (black).

In general the modeshapes (eigenvectors) with low eigenvalues are recognisably similar to those obtained for an annular duct at the same mean radius, whereas the higher order modes are not. This is illustrated in figure 7 and figure 8, which show unsteady pressure contours for the second cut-on upstream-travelling mode (the first is a simple plane wave) and the fifth cut-off upstream-travelling mode. Figure 7 shows a single circumferential lobe pattern throughout. The higher order mode in figure 8, however, shows a four lobe pattern near the outer wall and a two-lobe pattern near the inner wall, which cannot match any of the annular duct solutions for which the solution is separable in radius and circumferential angle.

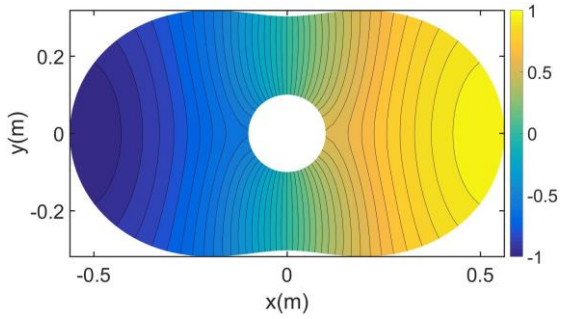

Figure 7. Second cut-on upstream travelling modeshape: real part of pressure profile normalised by pressure at the position of maximum amplitude.

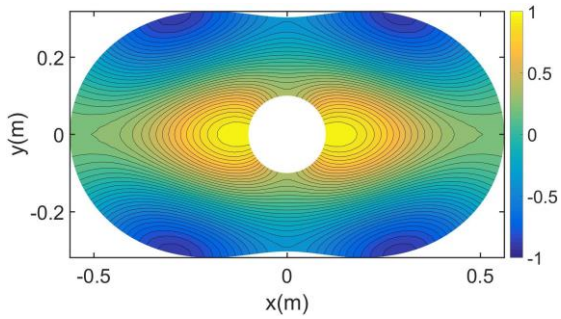

Figure 8. Fifth cut-off upstream travelling modeshape: real part of pressure profile normalised by pressure at the position of maximum amplitude.

6.2.5. *Semi-Analytic Calculation – Input and Output*

The sharp edges to the input pulse region (figure 5) cannot be accurately captured by the CFD mesh, and lead to minor non-physical effects in the immediate vicinity of the outlet plane. For this reason the input to the semi-analytic calculation was taken directly from the CFD solution at a position four axial planes upstream of the outlet.

Some manipulation was required to convert the CFD results into a form compatible with the semi-analytic calculation. Firstly ten snapshots were taken of the converged CFD solution and the first (time) harmonic calculated by Fourier transform. The velocity components were then transformed using the Jacobian matrix to the contravariant curvilinear vector basis used in the eigen analysis. A second Fourier transform was then applied in the η direction to transform the input pressure and velocity perturbations into the pseudo-spectral representation used in the analysis. These results were interpolated in ξ to the positions used in the semi-analytic calculation. Finally the inverse of the eigenvector matrix was used to convert the spatial representation into coefficients of each of the eigenmodes.

The input pressure profile on the outer wall is shown in figure 9. Only the upstream-travelling acoustic information, also shown in the figure, is utilised in the model. The small difference between the two represents the remnant of the spurious perturbation near the outlet boundary described previously.

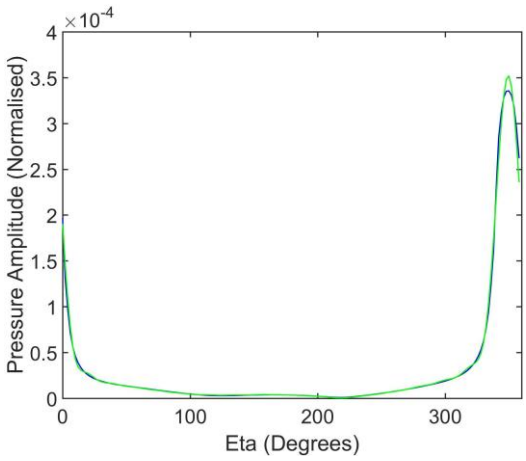

Figure 9. Input pressure profile: amplitude at the outer wall vs circumferential position η. The raw signal is shown in blue and the upstream-filtered signal in green.

The eigenmodes were propagated analytically, using the eigenvalues shown above, to a number of axial planes along the duct up to the test section inlet plane approximately one diameter upstream.

The reverse of the procedure described above was applied to the EAGCC results at each plane to allow them to be compared directly with the CFD solution.

6.2.6. *Results*

Figure 10 shows the unsteady pressure amplitude after propagation through the test section, again comparing the results of the semi-analytic calculation with the CFD results in terms of amplitude and phase. At this scale some differences are observable, but still relatively small.

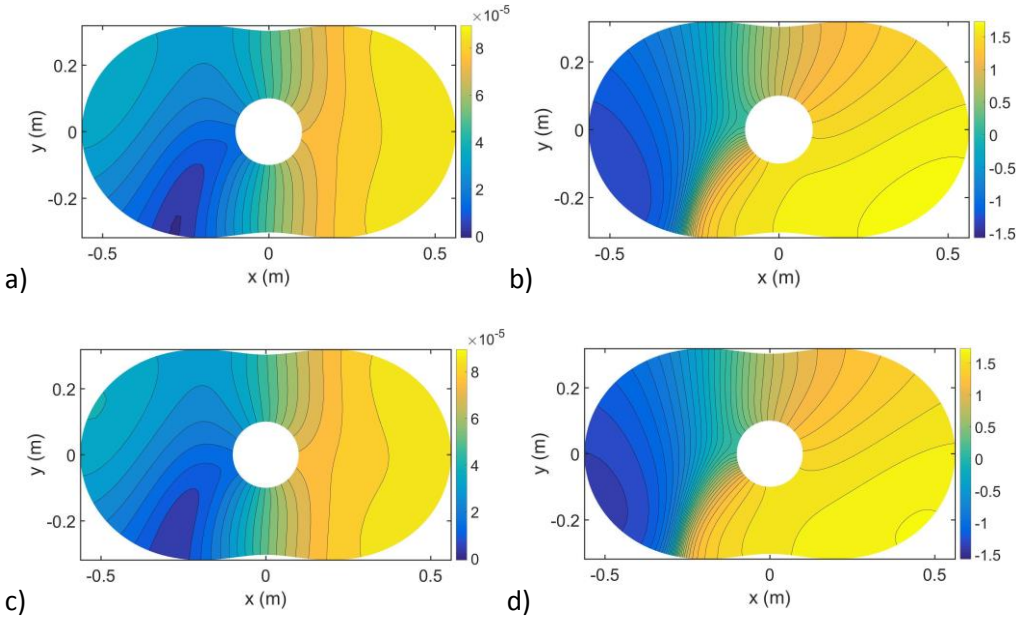

Figure 10. Pressure at the upstream end of the test section: a) Semi-analytic calculation, pressure amplitude (normalised), b) Semi-analytic calculation, pressure phase (radians), c) CFD calculation, pressure amplitude (normalised), d) CFD calculation, pressure phase (radians)

In order to quantify the differences, the pressure disturbances on the outer wall at the inlet plane are plotted in figure 11: The differences are seen to be small indeed – less than 2% in terms of maximum amplitude

difference and 0.05 radians of phase difference. At this level the difference may represent a small error in either the semi-analytic calculation or the CFD solution.

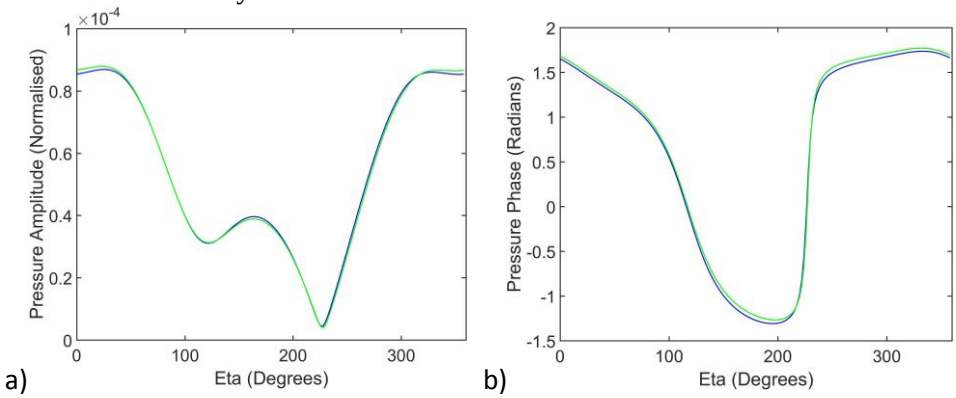

Figure 11. Pressure amplitude and phase vs circumferential position at the upstream end of the test section. The CFD result is shown in blue and the result of the semi-analytic calculation in green.

The above results show a direct comparison between the semi-analytic calculation and the validation solution. In the following graphs the CFD solution is "wavesplit" in the manner of Wilson [9] but using the eigenmodes calculated in the semi-analytic solution to demonstrate that the CFD solution follows in detail the behaviour predicted by the semi-analytic method.

Figure 12 shows amplitude and phase of the coefficients of the three cut-on modes compared with the linear behaviour predicted by the eigenvalue solution. Figure 13 shows the same for the first eight cut-off modes. In all cases the agreement is excellent.

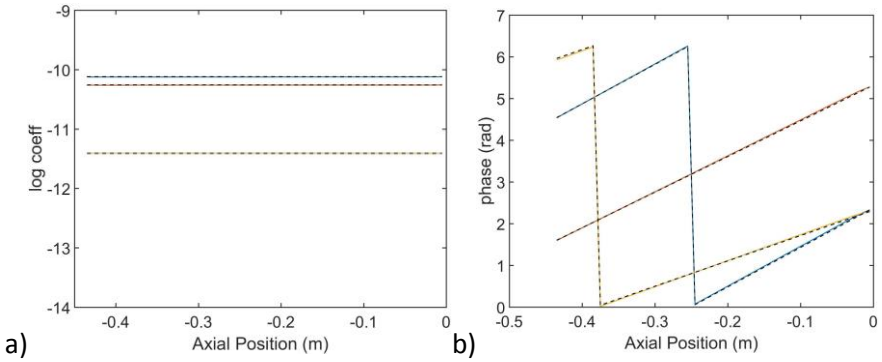

Figure 12. Log amplitude and phase of the coefficients of the cut-on upstream-travelling modes. Coloured lines show the coefficients as calculated from the CFD solution. Black dashed lines show the expected linear behaviour based on the eigenvalue for each mode.

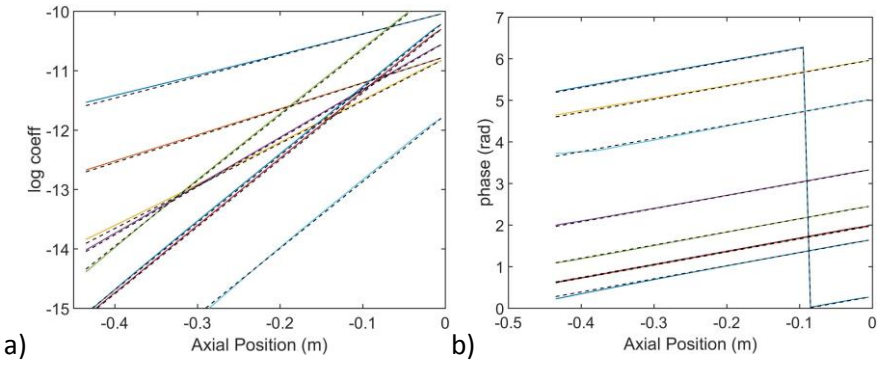

Figure 13. Log amplitude and phase of the coefficients of the first eight cut-off upstream-travelling modes. Coloured lines show the coefficients calculated from the CFD solution. Black dashed lines show the expected linear behaviour based on the eigenvalue for each mode.

6.3. *Validation Case 3: Extruded Non-Axisymmetric Annular duct and Non-Axisymmetric Mean Flow*

6.3.1. *Testcase Description*

The same geometry was used as for the previous testcase. In this case, however, the total pressure at the input plane was raised over a sector near top dead centre, leading to an increase in mean flow axial Mach number as shown in figure 14. The maximum Mach number, on the outer wall at top dead centre, was 0.6, compared with a value of 0.5 across the majority of the duct.

The total temperature was kept constant at the same levels used in validation case 2, and as a result there is a modest density variation around the duct, making the flow weakly non-homentropic. Both the general (non-homentropic mean flow) and the simplified forms of the method were applied: in this case no differences in the results were observed. The majority of the figures in this section were generated with the simplified method. Results with the general method are presented for comparison in figure 22.

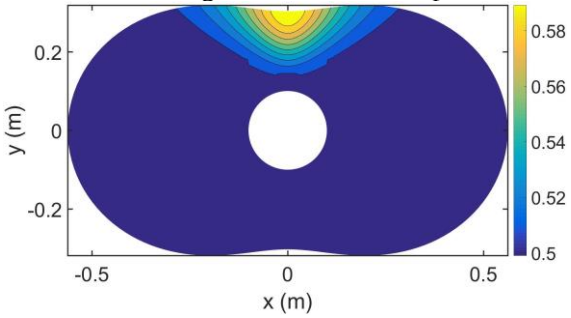

Figure 14. Validation case 3: Contours of mean flow Mach number.

6.3.2. *Eigenvalues and Modeshapes*

Figure 15a shows the eigenvalues calculated with the new non-uniform mean flow. As in the previous testcase these are presented as ζ-wavenumbers. Comparing this with figure 6 the low-order acoustic wavenumbers show only minor differences.

Figure 15b shows the equivalent results calculated using the general (non-homentropic mean flow) formulation. This figure shows, as expected, the addition of density-dominated (entropic) modes, shown in blue, clustered around the wave number associated with transport at mean flow speed. No differences can be observed, however, in the wavenumbers associated with acoustic and vortical modes.

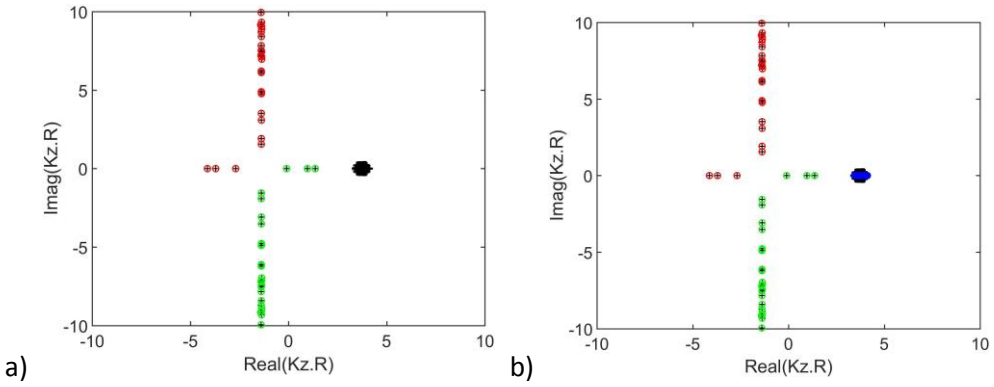

Figure 15. ζ-wavenumbers classified as upstream-travelling acoustic (red), downstream-travelling acoustic (green) and vortical (black). a) homentropic method, b) non-homentropic method, showing also entropic modes (blue).

The modeshape for the first cut-on acoustic mode is shown in Figure 16. With uniform mean flow (validation case 2) this was a plane wave, that is, uniform amplitude, and hence not plotted. Here, however, the pressure amplitude in the high-flow region is significantly higher than in the remainder of the duct (1.0 compared with 0.78 in normalised units).

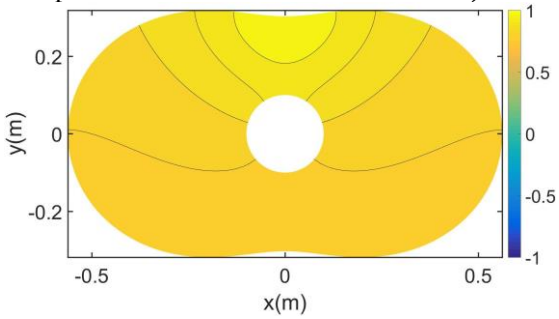

Figure 16. First cut-on upstream travelling modeshape: real part of pressure profile normalised by pressure at the position of maximum amplitude.

Figure 17 shows the second cut-on upstream mode, to be compared with figure 7, and figure 18 shows the fifth cut-off mode, for comparison with figure 8. The differences from the uniform flow case are surprisingly minor (neglecting +/- inversion, which has no impact on the analysis).

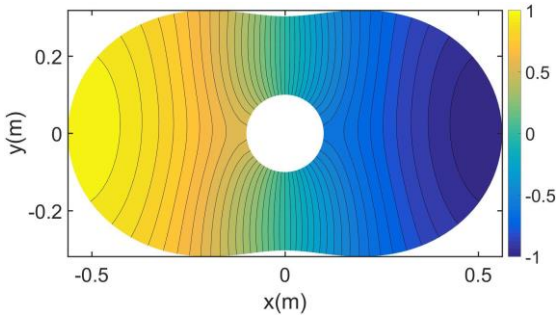

Figure 17. Second cut-on upstream travelling modeshape: real part of pressure profile normalised by pressure at the position of maximum amplitude.

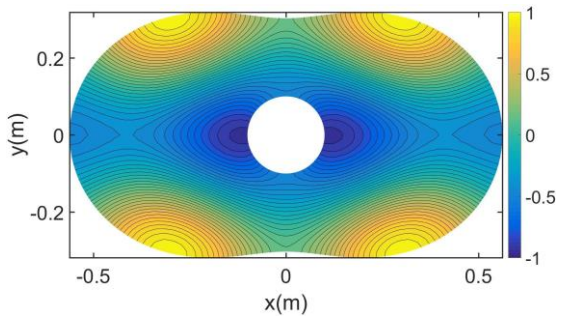

Figure 18. Fifth cut-off upstream travelling modeshape: real part of pressure profile normalised by pressure at the position of maximum amplitude.

6.3.3. *Results*

Figure 19 shows the amplitude and phase for the semi-analytic result compared with the CFD result for this case. Comparing with the results from the uniform flow case (figure 10), it can be seen that the non-uniform flow in this case has a relatively small effect.

The results along the outer wall are compared with the CFD solution in figure 20. The differences from the CFD solution are again small and appear to be systematic (that is, similar direction and size to those shown in figure 11 for the uniform flow case).

To isolate the effect of the non-uniform mean flow, figure 21 shows the ratio of the amplitude and the phase difference at each position on moving from the uniform to non-uniform flow case. It can be seen that the effects of the non-uniform flow are well captured by the current method.

Figure 22 shows the same information as the previous figure, but calculated with the general (non-homentropic mean flow) formulation. No significant differences can be observed from the simplified analysis in this case.

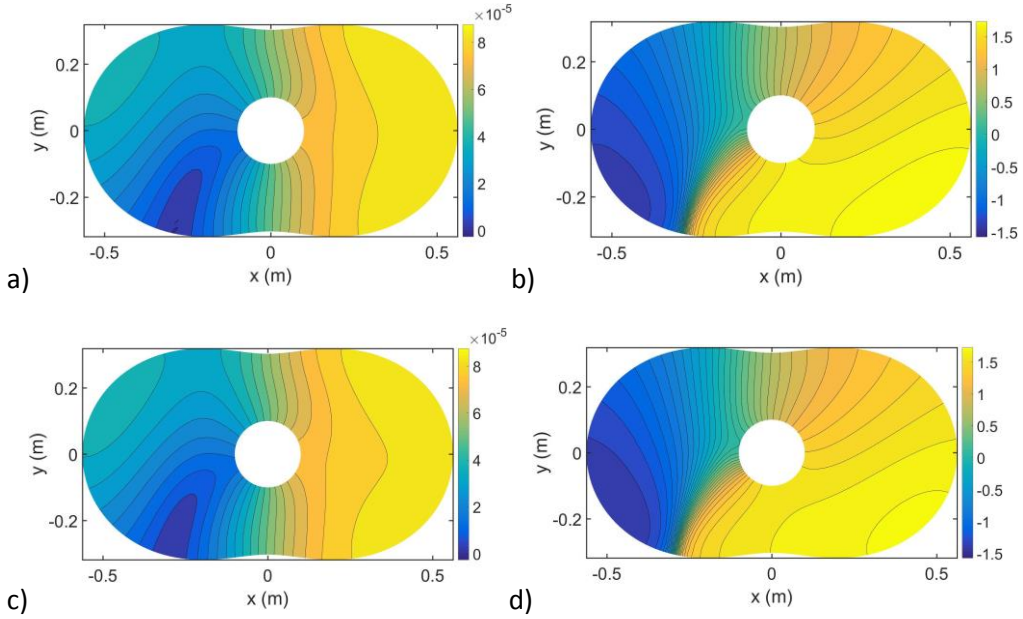

Figure 19. Pressure at the upstream end of the test section: a) Semi-analytic calculation, pressure amplitude (normalised), b) Semi-analytic calculation, pressure phase (radians), c) CFD calculation, pressure amplitude (normalised), d) CFD calculation, pressure phase (radians)

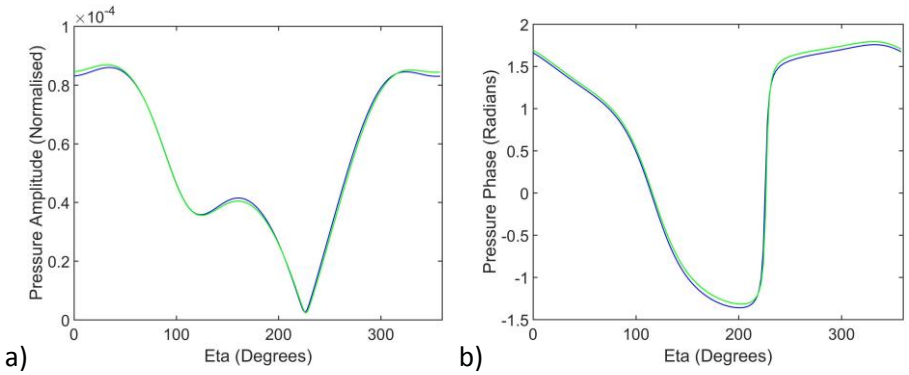

Figure 20. Pressure amplitude and phase vs circumferential position at the inlet to the test section. The CFD result is shown in blue and the result of the semi-analytic calculation in green.

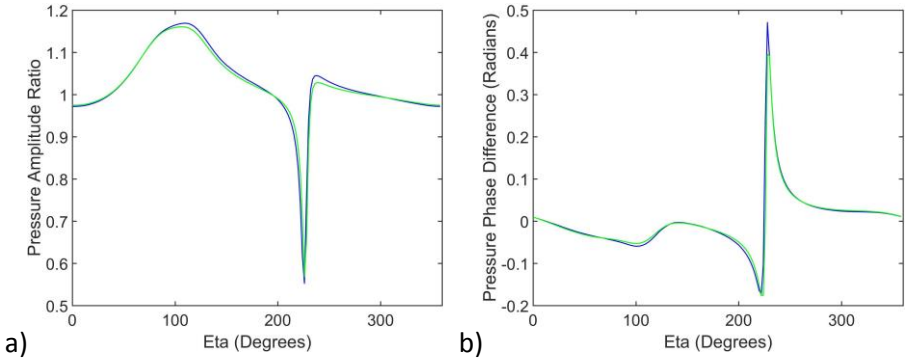

Figure 21. Pressure amplitude ratio and phase difference on moving from the uniform flow to the non-uniform flow case. The CFD result is shown in blue and the result of the semi-analytic calculation in green.

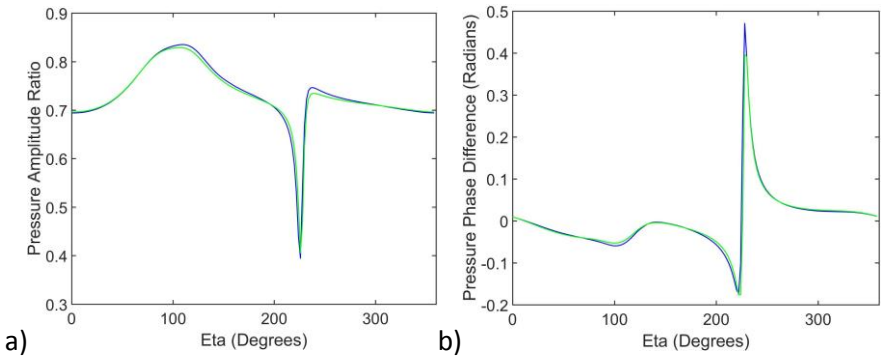

Figure 22. Repeat of previous figure calculated using the general (non-homentropic mean flow) formulation.

6.4. *Validation Case 4: Axially and Circumferentially Non-Uniform Duct and Mean Flow*

6.4.1. *Case Description and Validating CFD calculation*

The test section consists of a curved cylindrical annular duct, with straight ducts at inlet and outlet (figure 23). It is qualitatively similar to that chosen by Prinn et al [25] as a stepping stone towards a full aeroengine inlet duct geometry.

The inner and outer radii for this test case match those of validation case 1 (0.1m and 0.432m respectively). The curved section (shown in red on figure 23) is 0.5 duct diameters long (measured along the centreline) and curves at a uniform rate through 16.42 degrees.

The mean flow was calculated using CFD in inviscid mode, hence the mean flow in this case is irrotational, although that feature is not used in the analysis. The inlet total pressure and exit static pressure were held constant across the duct, at a ratio consistent with a Mach number of 0.5.

The test case itself involved the introduction of a low amplitude rotating pressure signal at duct outlet. This signal took the form of a first radial order Bessel-Fourier mode at circumferential order m=4 and angular velocity consistent with a rotational Mach number at the outer wall of 1.2; if the duct and mean flow were axially uniform this mode would be cut-on and propagate at uniform amplitude along the duct. A low circumferential order input disturbance was deliberately chosen to minimise the computational expense of the CFD calculation used to validate the results.

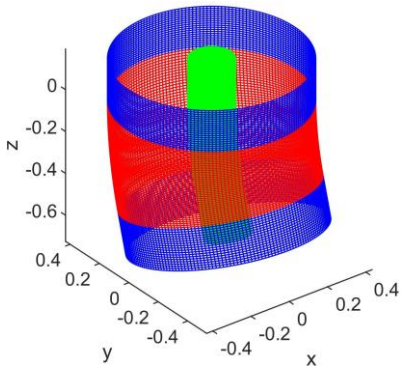

Figure 23. Validation case 4 geometry. The curved section is highlighted in red and the straight sections in blue. The validating CFD calculation included an additional damping region, not shown, at the inlet (see text).

The same CFD calculation was used to provide the mean flow as well as validating the calculation of the unsteady perturbation. The CFD mesh on the inner and outer wall of the test section is illustrated in figure 23. It was hexahedral, with 31 points equispaced in the radial direction, 180 points in the circumferential direction and 87 points along the duct, giving approximately cubic cells around mid-span in the straight sections. The mesh on the curved section was generated by extruding along the mean line as shown in the figure.

This mesh definition is sufficient to capture the propagation to within a fraction of a dB, although it will be shown later that there is still a small level of dissipation error present.

An additional mesh was added to the inlet to damp reflections from the inlet boundary. This mesh was extruded from the inlet plane with 26 additional axial points, but increasing the axial mesh spacing at an expansion ratio of 1.2.

6.4.2. *Mean Flow*

The mean flow as calculated by the CFD calculation is shown in figure 24. Velocity and gauge pressure are plotted on a plane through the axis of the curvature of the duct. As expected, low velocities and high pressures are seen in the outer region and vice-versa in the inner region.

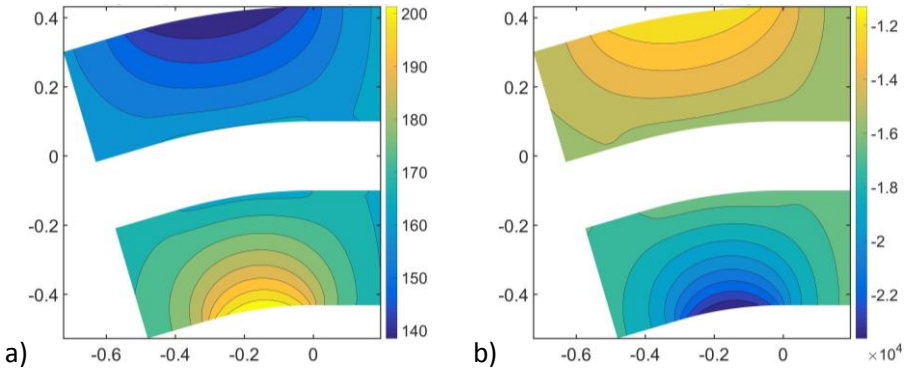

Figure 24. Mean flow a) Velocity (m/s) and b) Gauge pressure (Pa)

6.4.3. *Coordinate System for Eigen Analysis*

The blue lines in figure 25 show the EAGCC mesh compared to a cut through the CFD mesh. For clarity only 11 ζ-planes are shown on the EAGCC mesh and every 10th axial position on the CFD mesh. The CFD mesh is in fact an orthogonal mesh, and indeed this particular problem could be solved by splitting the mesh into three zones and performing a conventional eigenvalue solution in each zone, but the result would not then be extendable to general duct shapes.

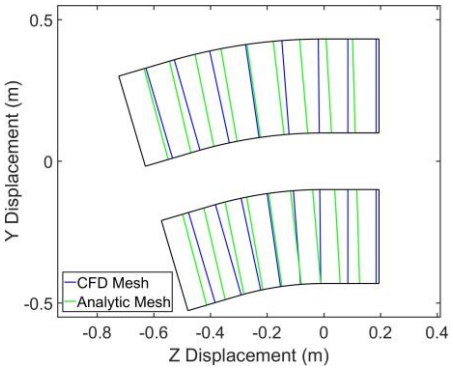

Figure 25. Cut through the CFD mesh (every 10th point shown) and the EAGCC Mesh at Similar Definition. Only pseudo-axial lines are shown.

Although the CFD mesh is orthogonal, it would *not* be a good choice as the curvilinear coordinate system in the present analysis method for reasons that are considered later. In this case the analytic mesh was derived from the CFD mesh by simply equispacing the points in ζ while leaving ξ and η fixed (that is, sliding the points along the CFD ζ-lines until equispaced). The result of this is a more uniform mesh spacing, but it also leads to analysis planes that are no longer orthogonal to the geometry, as illustrated by the green lines in figure 25.

Most of the results presented in the following sections were calculated using 26 analysis planes, but in order to assess the convergence of the method with axial definition results were also obtained using 5, 11, 51 and 101 analysis planes. In each case the Jacobian and metric tensors were calculated on the finest mesh to avoid unnecessary discretisation errors.

6.4.4. *Input perturbation*

The input perturbation was taken from the CFD solution at the downstream end using the procedure described for validation case 2. A similar process was used to provide input to the two-way sweep method at the

upstream end of the test section. This was again done at a single plane, and the result propagated in the reverse sweep.

6.4.5. *Results*

Figure 26 shows a direct comparison between the results of the two-way sweep method applied on 26 zeta planes and the CFD solution, in terms of pressure in the plane of curvature of the duct centre-line. It can be seen that the results are almost identical.

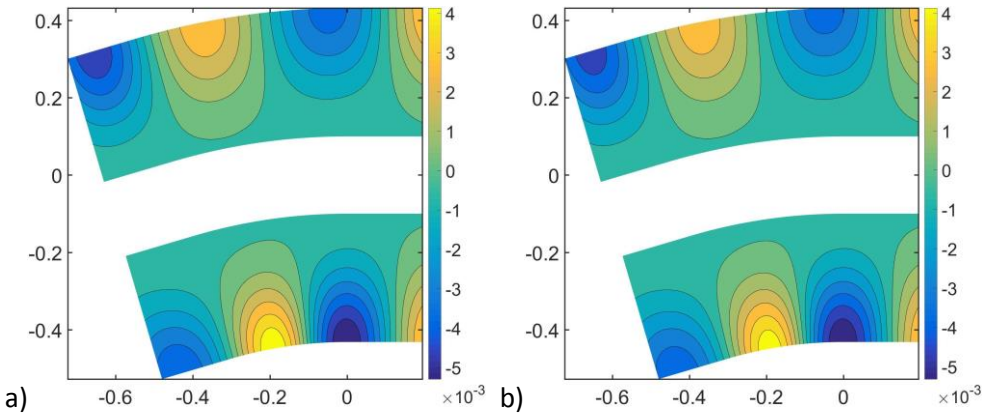

Figure 26. Pressure contours (normalised) (a) Semi-analytic two-way sweep method (b) Validating CFD calculation

It will be seen below that the CFD solution includes some reflection from the inlet region, despite the presence of the damping zone. For this reason it is not sensible to compare the results of the one-way calculation directly with the CFD solution (although that comparison can be found in the modal amplitude results presented later). Instead the CFD results are first filtered using the calculated eigenmodes, retaining just the upstream-travelling information.

Figure 27 shows a comparison in terms of static pressure between the one-way semi-analytic solution and the upstream-filtered CFD solution. Again the results are nearly identical with each other, and both slightly modified from the full CFD and two-way sweep results shown in the previous figure.

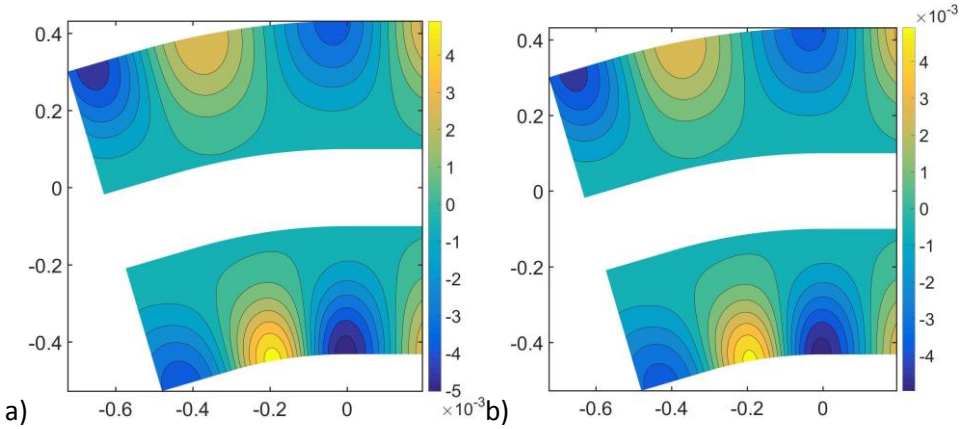

Figure 27. Pressure contours (normalised) (a) Semi-analytic one-way sweep Method (b) Upstream-filtered CFD result

Figure 28 compares static pressure results from both semi-analytic models and the CFD results at the upstream plane after propagation through the test section. The small differences between the filtered and unfiltered CFD results show the effect of the reflections, both at inlet and through the test section, which are seen to be well captured by the two-way model.

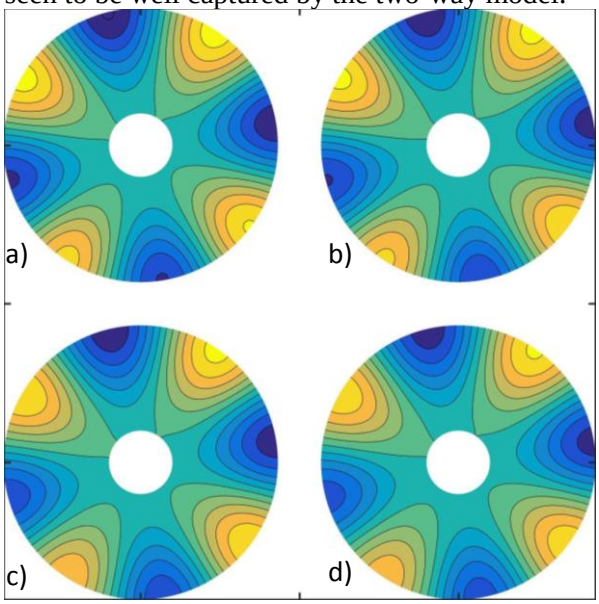

Figure 28. Perturbation Pressure (normalised) at the (upstream) inlet to the test section: a) Two-way sweep b) CFD c) one-way sweep d) Upstream filtered CFD.

The results are extremely similar to the CFD solutions – to the point where it can be stated that there is no qualitative difference between the semi-analytic and the CFD results.

Figure 29 shows the one-way sweep and the upstream filtered CFD results in terms of circumferential harmonic pressure coefficients at the outer wall at inlet and outlet. In the semi-analytic case the pressure on the wall has been reconstructed from the eigenmodes (which are not pure circumferential harmonics due to the duct curvature and mean flow variation) on a circumferentially uniform mesh and then Fourier transformed in the circumferential direction.

The input signal is strongly dominated by circumferential harmonic m=4, which was the target input signal – small elements of m=3 and m=5 come from the interaction of the vestigial mean flow variation with the outlet boundary condition. The non-uniform geometry and mean flow in the test section scatters the pressure signal into other harmonics. This can be clearly seen in the lower orders (m=2 and m=3). It is less clear in the higher orders (m=5 and m=6); this is because the modes most closely related to these harmonics are cut-off (that is, decay with upstream distance). The base signal is continually scattered into these modes, but the amplitude immediately decays again.

Figure 30 shows the same information for the two-way sweep method and the unfiltered CFD signal. Again the difference between the CFD and the semi-analytic solution is very small. Comparing with figure 29 it can be seen that the effect of the two-way sweep is small but significant at the downstream end. Close inspection of the graphs reveals some difference also at the upstream end. Comparison with the filtered CFD solution (as shown in Figure 28), however, shows that this difference is not due to multiple reflections within the domain but from reflections from the stretched mesh upstream of the test section in the CFD calculation, which are neglected in the one-way sweep calculation.

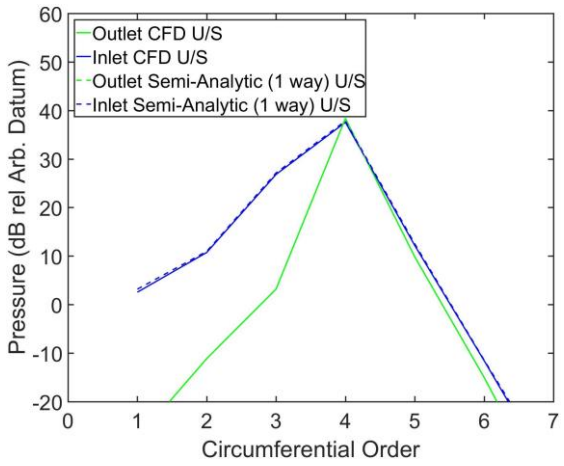

Figure 29. Pressure on the outer wall at inlet and exit calculated using the one-way sweep method, decomposed into circumferential harmonics. The CFD results are upstream-filtered. The signal at outlet (shown in green) is an input to the semi-analytic model, and hence by definition agrees with the CFD solution.

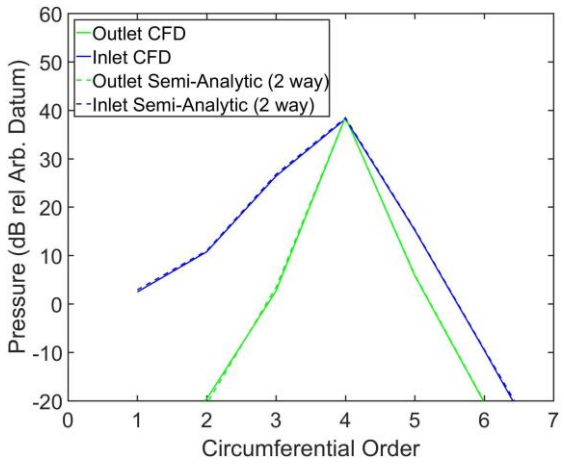

Figure 30. Pressure on the outer wall at inlet and exit calculated using the two-way sweep method, decomposed into circumferential harmonics. The CFD results are unfiltered.

The simple geometry of this testcase makes it possible to construct similar information (circumferential harmonics of pressure at the outer wall) all the way along the test section. The simplest way to do this was to interpolate the semi-analytic results back onto the CFD mesh, which consisted of a series of circular annular cross-sections perpendicular to the (curved) duct centreline. The results are shown for circumferential harmonics m=3 to m=5 in figure 31 for the one-way Sweep method, and figure 32 for the two-way sweep method. The variable on the x axis is the index in the CFD mesh: these positions are equispaced along the (curved) centre-line of the duct. In both figures the boundaries between the curved and straight parts of the duct are clearly visible from the "corners" in the scattered harmonic amplitudes at axial positions 20 and 63.

One immediate conclusion from these graphs is that the scattering behaviour is complex; this might be expected given that a) the rate of change in harmonic amplitude at any point is a combination of local scattering and propagation of previously-scattered waves and b) the mean flow changes continuously throughout the test section. The semi-analytic results follow the CFD results throughout, demonstrating that both of these effects are well captured in the current method.

The changing amplitudes in the straight duct regions at either end of the test section show that the signal is scattered by the mean flow as well as the geometry. At a simplistic level the sharp change in behaviour at the

"corner" points demonstrates that the geometry also plays a part in scattering the signal. Although this is true in the sense that it affects the upstream acoustic field, the physical interpretation is not so clear: the path length between adjacent mesh nodes along the inner part of the curve is shorter than the path length at the outer part, and the effect of this path length change is conflated with reflection effects from the wall curvature and scattering by the mean flow. This illustrates the important fact that even for very simple geometries part of the apparent scattering is a direct result of the coordinate system in which the results are analysed (see under Choice of Coordinate System in the Discussion section).

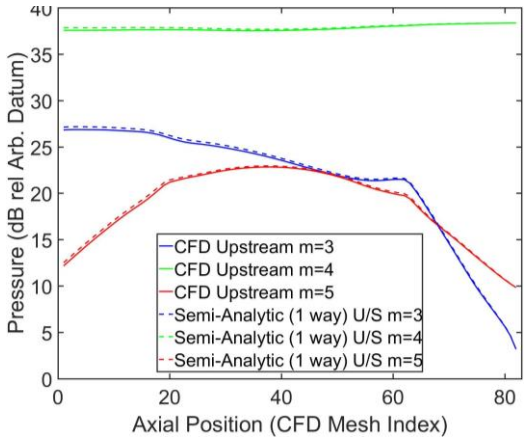

Figure 31. Pressure along the outer wall calculated with the one-way sweep method interpolated onto the CFD mesh and decomposed into circumferential harmonics. The CFD results are upstream-filtered.

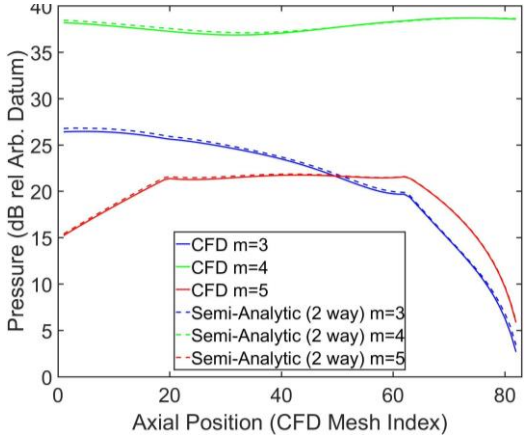

Figure 32. Pressure along the outer wall calculated with the two-way sweep method interpolated onto the CFD mesh and decomposed into circumferential harmonics. The CFD results are unfiltered.

The effect of pseudo-axial discretisation is shown in figure 33 for the One-Way Sweep method. Even with 5 analysis planes the maximum error relative to the CFD solution on the outer wall is of the order of 1dB, and that in mode 5 which is itself low amplitude at the inlet plane (figure 29). The maximum error using 11 analysis planes is of the order of 0.5dB, and there is little improvement from using additional planes.

The error level observed in figure 33 is of the same order as the dissipation error in the validating CFD solution. Detailed analysis of the results along the duct shows that the apparent error grows approximately linearly with distance along the duct (as can be seen in figure 31), which is consistent with a level of dissipation error in the validating solution.

Nonetheless, the results demonstrate that no more than eleven analysis planes are required in this case to obtain a solution accurate to within 0.5dB.

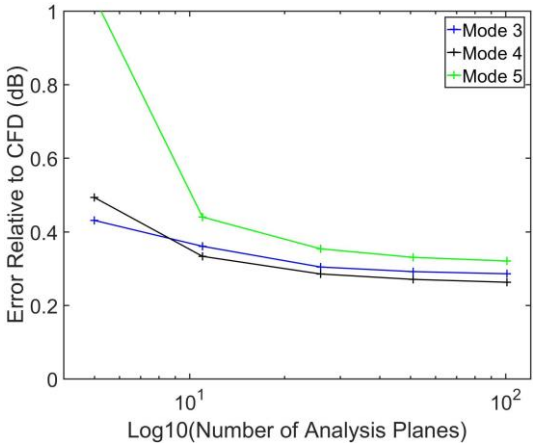

Figure 33. Pressure at the outer wall at the upstream end of the test section calculated using the one-way sweep method decomposed into circumferential harmonics 3, 4 and 5 and plotted as abs(ΔdB) relative to the upstream-filtered CFD result. The symbols represent calculations with 5, 11, 26, 51 and 101 analysis planes.

6.4.6. *Calculation Time*

The calculations presented in this paper were performed in MATLAB (Version 2015a) on a 4-core desktop pc with Intel® Core™ i7-4790 cpus rated at 3.60GHz. The times presented in this section are for validation case 4, with 26 analysis planes. Pre-processing in this case was performed in serial mode, whereas the eigenvector/eigenvalue calculations themselves were performed in parallel mode using 7 virtual processes.

The pre-processing stage is defined as the time spent building the matrices A and B in equation 23 for each analysis plane in turn. The time spent in this stage is expected to be considerably higher than with conventional analysis due to the large number of terms that have to be collated. The matrices in the eigenvector/eigenvalue calculation, on the other hand, are the same size as those derived in orthogonal coordinate systems, and hence the solution time should be similar in the two cases, although it is noted that the matrices based on orthogonal coordinate systems are more sparse, which may be of advantage using some solvers.

Neglecting the time required for loading and interpolating the CFD data, pre-processing of the equations took just under 25 seconds. The eigensolution itself, even performed in parallel, took 133 seconds. The validation CFD calculations, for comparison, running on the same machine but in parallel, took several days elapsed time to reach cycle convergence.

These figures show that the bulk of the analysis time is taken up by the eigenvalue/eigenvector calculation itself. The extra computation required for the general curvilinear coordinates appears in the pre-processing step, which accounts for only one sixth of the total calculation time.

The matrix for which eigenvalues are sought is of size $\left(n_{equ}n_{\xi}n_{m}\right)^{2}$ where n_{ξ} is the number of points in the pseudo-radial direction, n_{m} the number of pseudo-spectral modes in the circumferential direction and n_{equ} the number of equations (4 for the homentropic mean flow solution and 5 for the general case). Given that the computational requirement for calculating eigenvectors is strongly non-linear with matrix size, any eigen-based method will hit a limit in terms of the mesh definition that can be achieved, and hence the wavelength that can be captured. This data, however, shows that the *incremental* computational cost of using this method over a conventional eigen-based method is small.

6.5. *Validation Case 5: Axisymmetric Horn*

6.5.1. *Case Description and Validation Results*

Case 4 provided a comprehensive validation of the EAGCC method using the two-way sweep methodology, but direct comparison was hindered by reflections in the validating CFD solution. In order to obtain a more direct assessment of the two-way sweep method a fifth validation case was added, based on measurements and calculations performed by Post and Hixson [26] on an axisymmetric Tractrix horn.

The horn geometry is shown in Figure 34. The length of the horn is 0.559m. The radius at the throat is 0.0254m and at the mouth 0.271m. The mouth is flanged as shown in the figure. There is no mean flow in the duct.

Post and Hixson [26] measured the impedance at the throat, comparing with numerical calculations using a boundary element method. Good agreement (reproduced later in the results section) was found for modest ka values (less than about 5), where ka is defined as the free-space wavenumber multiplied by the mouth radius.

6.5.2. *Coordinate System for Eigen Analysis*

The mesh used in the analysis is shown in Figure 34. Because the current method is set up for annular rather than cylindrical ducts an artificial inner wall has been added at radius 0.001m; this is considered sufficiently small to have negligible effect on the calculated results.

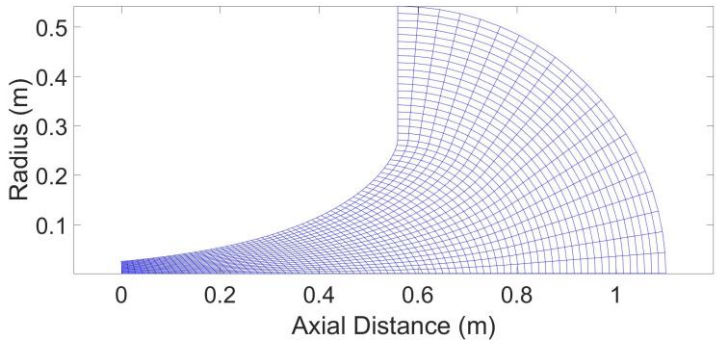

Figure 34. Geometry and analysis mesh for validation case 5 (Tractrix horn).

The mesh has 21 points in the pseudo-radial direction and 80 points in the pseudo-axial direction. The Tractrix horn by definition can be defined using a succession of circular arcs normal to the walls: this would *not* make a good mesh for eigen analysis, however, and was not used here, because the mesh points on the outer wall become almost coincident at the mouth: this would give high gradients in the jacobian and metric tensor, which leads to eigenmodes that vary strongly with axial position, and hence high errors when integrating in the pseudo-axial direction. Instead, the points on the outer wall were equispaced to give the smoothly varying mesh shown in the figure. As a result the mesh is no longer orthogonal to the outer wall.

6.5.3. *Input perturbation and impedance calculation*

The only cut-on modes in the eigensolution are those with approximately constant pressure along lines of constant zeta. Accordingly the input used was a single downstream mode at the inlet plane. In general the reflected wave had at the throat approximately constant pressure, but to reduce the result to a single value the pressure and the normal velocity were area averaged over the inlet plane and the averaged results used to calculate the impedance.

6.5.4. *Results*

Results were obtained for a range of frequencies between ka=0 and ka=5. Within this range the two-way sweep method failed to converge at various points – most notably between ka=1.0 And ka=1.9. At these ka values the eigen analysis predicted a region of cut-off waves part-way along the horn; further work is required to achieve convergence at these conditions.

Figure 35 shows an example of the results (ka=4.5, where the results converged successfully) in terms of static pressure profile.

The throat impedance (in terms of resistance and reactance) was calculated for all of the frequencies at which convergence was achieved and is shown in Figure 36. Also shown for comparison are the results of the one-way sweep method which is clearly insufficient for this geometry.

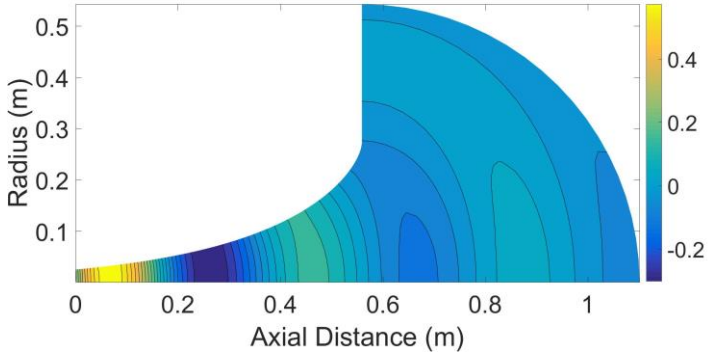

Figure 35. Tractrix horn: real part of static pressure (non-dimensional) at ka=4.5.

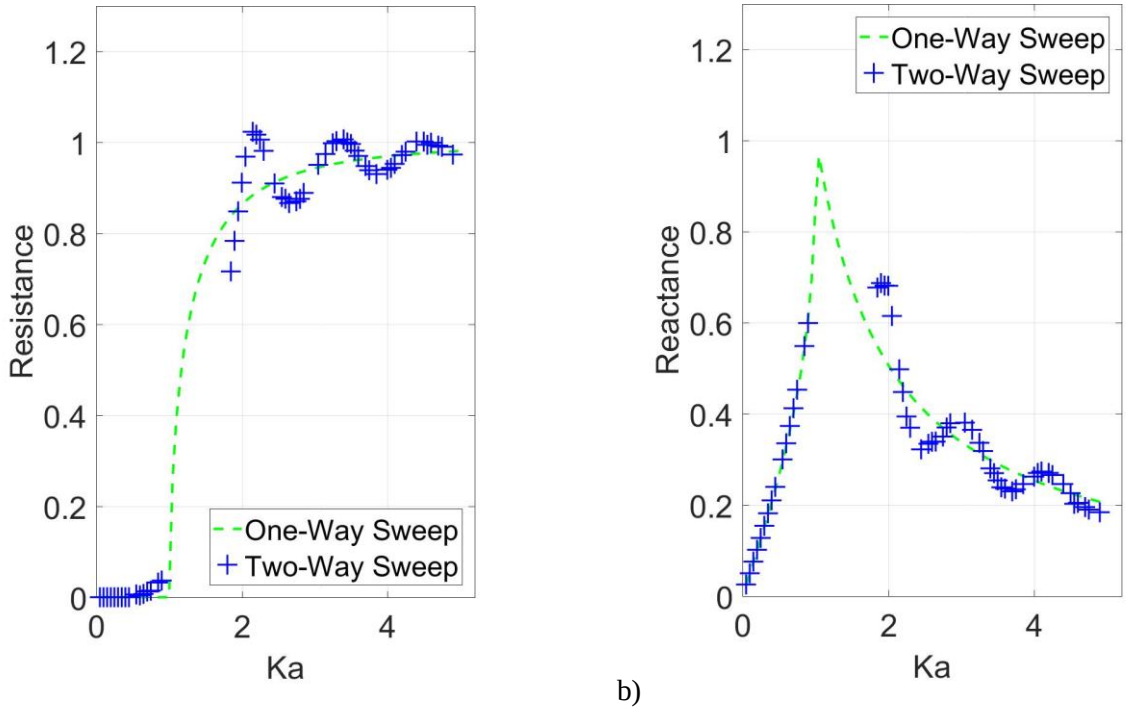

a) b)

Figure 36. Tractrix horn resistance (a) and reactance (b) at the throat. Blue crosses represent results from the current method, for comparison with figures 4.28 and 4.29 of Post and Hixson [26]. Also shown are results using the one-way sweep method (green dash line).

The EAGCC method agrees almost exactly with the results of the boundary element method presented by Post and Hixson [26], and like their solution agrees reasonably well with the measured results they present.

The wavy character of both resistance and reactance above ka=1 is the result of axial reflections, as can be seen from the fact that the "one-way" solution varies smoothly with frequency. This case thus validates the capability of the EAGCC method to capture reflections in a strongly varying duct.

7. Discussion

7.1. *Accuracy*

The results in the previous sections provide a basic validation of the eigenvector method in general curvilinear coordinates for acoustic propagation in general hardwall ducts of non-uniform shape with non-uniform mean flow. In all cases results are achieved down to the same level of accuracy as the validating CFD solutions.

Both the one-way and the two-way sweep methods are shown to be accurate. The one-way sweep method corresponds to the axial integration method used in previous analyses for slowly-varying ducts in which it was assumed that reflections in the duct and at inlet are sufficiently small that they do not re-reflect to contaminate the upstream acoustic field, and this assumption is shown to hold for the first four validation cases described here. The two-way sweep method extends this capability to cases, such as test case 5, with more significant variation of geometry and/or mean flow and where reflected waves can be significant.

In validation case 4 the effect of discretisation in the ζ direction was investigated, and it was found that results accurate to approximately 1dB were obtained using only five analysis positions. This surprising result is due to the choice of coordinate system which is discussed below.

7.2. *Computational Expense*

The calculation times presented for validation case 4 show the method to be efficient in terms of computational expense. In particular the incremental expense of using general curvilinear coordinates is shown to be small relative to previous approximate methods using orthogonal coordinate systems. Furthermore, the freedom to choose an appropriate coordinate system can lead to a significant reduction in the overall computational expense relative to those methods (see section following).

In the general case with modeshapes that vary with axial position one might consider what benefit the eigen analysis brings over a boundary element or volumetric calculation. The following features are preserved from the conventional analysis in orthogonal coordinate systems and contribute to the efficiency of the current method:

1. Each eigenmode can be associated a propagation direction (+/- in the ζ coordinate). This allows the perturbation field to be calculated in a "one-way sweep" in cases where reflections can be neglected.
2. The eigenmode coefficients can be propagated analytically, removing the "points-per-wavelength" limit encountered with numerical volumetric discretisation schemes and hence allowing larger spatial steps in the propagation direction. In axially non-uniform ducts the step size is instead limited by changes in geometry, mean flow and/or the Jacobian of the coordinate system.
3. The use of a boundary-fitted curvilinear mesh simplifies the use of high-order approximation of derivatives with respect to the non-constant coordinates (ξ, η) in each plane. This reduces the size of the matrices needed for the eigen analysis and hence improves the speed of calculation.

4. With appropriate choice of coordinate system a spectral method can often be used in the pseudo-circumferential direction, even for non-axisymmetric ducts.
5. The boundary conditions in the propagation direction are automatically non-reflective, removing the need for any additional treatment or reflection damping zones.
6. Only one (curved) plane of information is analysed at a time, avoiding the very large matrix operations associated with boundary element methods.

The timings reported for validation case 4 indicate that the current method is substantially faster than the validating volumetric CFD calculation. This has been confirmed by Wilson [23] for calculations using a representative aeroengine inlet duct, where the computational expense was shown to be 0.25% of that required for an equivalent CFD calculation.

The bulk of the computational requirement is taken in the eigen solution itself, which is highly, and non-linearly, dependent on the size of the matrices involved. This makes the current method unsuitable for calculations requiring highly refined meshes in the (ξ, η) plane. During the course of the current work, with the compute hardware described in section 6.4.6, a rough practical limit was found to be $n_{equ} n_{\xi} n_m < 5000$, at which point the eigen solution on a single analysis surface takes approximately one hour. This matrix size is sufficient for complex ducts and geometry (as demonstrated by Wilson [23]) at low to moderate wavenumbers provided that wall boundary layers can be neglected. Conversely it would also be sufficient for calculations including a wall boundary layer if the geometry and mean flow are axisymmetric.

In all cases each analysis surface is treated independently. Hence the computational cost is only linearly related to the number of surfaces used, and furthermore parallelisation of this aspect is trivial, in that each eigensolution can be performed on a separate processor.

7.3. *Choice of Coordinate System for Eigen Analysis*

The discussion on path length in validation case 4 highlights an important issue with respect to the choice of coordinate system. Referring back to figure 25, although the CFD mesh is orthogonal, it would *not* be a good choice as the basis for the curvilinear coordinate system. This is because the eigensolutions in curvilinear coordinates depend not only on the geometry and mean flow (which in this case are both smoothly varying) but also on the metric tensor, which is a function of the chosen curvilinear coordinate system. In this case the metric tensor has a discontinuity at the boundaries between the straight and curved sections, as evidenced by the change in axial spacing at the outer walls of the duct highlighted in figure 25.

In a conventional analysis, such as described by Brambley and Peake [6], the analysis planes are fixed by the duct geometry, and the discontinuity in the metric tensor cannot in general be avoided – instead regions of high gradient in the metric tensor have to be finely meshed with consequent increase in computational expense.

It is important to note that the discontinuity in the metric tensor, and the difficulties that arise from it, are *not* a function of the duct geometry or the mean flow, but rather of the coordinate system chosen to address the problem.

With general curvilinear coordinates it is possible to choose a coordinate system to optimise computational efficiency, and in general this means that the coordinate system itself should be as smooth as possible. The leading error terms in the propagation method relate to differences in the eigensolutions calculated at successive analysis planes, and these differences can be minimised by adopting a coordinate system that not only removes discontinuities in the metric tensor, but makes it as smooth as possible in the ζ direction.

In validation case 4 an optimised coordinate system was generated for the semi-analytic calculations by smoothing the CFD mesh explicitly in the ζ direction. The benefit of this is seen in the fact that results accurate to 1dB were obtained with only 5 calculation planes along the duct.

8. Conclusions and Future Work

Eigen analysis in general curvilinear coordinates (EAGCC) offers a fast, accurate method for prediction of linear acoustic perturbations in three-dimensional non-uniform ducts with non-uniform mean flow.

Validation has been performed for prediction of acoustic waves in uniform and non-uniform ducts with uniform and non-uniform but irrotational and (nearly) homentropic mean flow.

Previous approaches were subject to limitations on geometry and mean flow (for instance slowly-varying ducts) that are not required in the current method, for which the only limitations are that the duct and mean flow vary smoothly with position.

The underlying equations are more complex than previous more approximate treatments using orthogonal coordinate systems, and the use of symbolic manipulation is recommended. The analysis time, however, is similar to that required for previous methods, and for the calculations presented between two and four orders of magnitude smaller than that required for CFD analysis using a conventional low order RANS solver.

In previous approaches the analysis surfaces were predetermined by the geometry, which can lead to steep gradients in the metric tensor. In these cases high definition is required in the propagation direction leading to high computational expense. This is an artificial problem, which can be mitigated in the current system by choosing a coordinate system to minimise these gradients.

The addition of the two-way sweep method extends the range of application to cases where internal reflections are significant. Convergence issues were observed in axisymmetric calculations where cut-off occurs part-way along the duct.

Future work is required to make the calculation method more robust, both in terms of a robust method for determining the direction of travel of eigenmodes in the general case and to counter the instabilities in the two-way sweep method observed at some frequencies in testcase 5. The current work includes an element of error analysis but a more formal analysis is required of errors related to how well the mesh in the ζ direction captures changes to the eigenvectors along the duct. The method will be extended to include an acoustic liner boundary condition at the duct walls and a radiation method for calculating farfield noise. Validation will be extended to include propagation of linear vortical and entropic disturbances as well as acoustic propagation in rotational and non-homentropic mean flows.

Acknowledgements

The latter part of this work was completed with the support of the Innovate UK Aerospace Technology Institute through the funded research program ACAPELLA (Advanced Capability for Prediction of Engine Level Acoustics, ref.113086). The author would also like to thank Professor Jeremy Astley for casting a critical eye over the early drafts of the paper and making many helpful suggestions.

Appendix A. Identities Used in Derivation of Tensor Equations

The following equations are derived from basic identities to be found in standard textbooks on tensor calculus such as Spain [27]).

$\nabla \cdot \boldsymbol{u}' \equiv \nabla_i u^i = \frac{1}{\sqrt{g}} \frac{\partial}{\partial x^i} \left(\sqrt{g} u^i \right)$ where $g = \left| g_{ij} \right|$ and g_{ij} is the metric tensor. (Eq. 43)

This is the Voss-Weyl formula, but presented anonymously in Spain [27], p32.

In terms of covariant velocity vector u_j this can be written

$\nabla \cdot \boldsymbol{u}' = \frac{1}{\sqrt{g}} \frac{\partial}{\partial x^i} \left(\sqrt{g} g^{ij} u_j \right)$, where g^{ij} is the inverse of the metric tensor matrix g_{ij}. (Eq. 44)

$(\boldsymbol{a} \times \boldsymbol{b})_i = g_{il} \epsilon^{ljk} a_j b_k$ (Spain [27], p61) (Eq. 45)

where the permutation tensor ϵ^{ljk} is defined in terms of the permutation symbol e_{ljk} by

$\epsilon^{ljk} = \frac{1}{\sqrt{g}} e^{ljk}$ (Spain [27], p59) (Eq. 46)

$(\nabla \times \boldsymbol{u})_{\mathrm{i}} = g_{il} \epsilon^{ljk} \frac{\partial u_k}{\partial x^j}$ (Spain [27], p61) (Eq. 47)

$(\boldsymbol{u} \cdot \nabla \phi) = g^{ij} u_j \frac{\partial \phi}{\partial x^i}$ (Eq. 48)

$(\boldsymbol{u} \cdot \nabla \boldsymbol{u}) = \nabla \left(\frac{1}{2} \boldsymbol{u} \cdot \boldsymbol{u} \right) - \boldsymbol{u} \times (\nabla \times \boldsymbol{u})$ (Eq. 49)

Hence, using the equations above for cross-product and curl,

$(\boldsymbol{u} \cdot \nabla \boldsymbol{u})_{\mathrm{i}} = \frac{1}{2} \frac{\partial}{\partial x^i} \left(g^{jk} u_j u_k \right) - \epsilon^{ljk} \epsilon^{mnp} g_{il} g_{km} u_j \frac{\partial u_p}{\partial x^n}$ (Eq. 50)

References

1. J.M. Tyler, T.G. Sofrin, Axial Flow Compressor Noise Studies. Trans. Soc. Automotive Engineers 70(1962), 309–332.
2. S.W. Rienstra, Sound Transmission in Slowly Varying Circular and Annular Lined Ducts with Flow. J. Fluid Mech. 380(1999), 279-296.
3. N. Peake, A. Cooper, Acoustic Propagation in Ducts with Slowly Varying Elliptic Cross-Section. J Sound Vib. 243 (3)(2001), 381-401.
4. S.W. Rienstra, Sound Propagation in Slowly Varying Lined Flow Ducts of Arbitrary Cross-Section. J. Fluid Mech. 495(2003), 157-173.
5. R.J. Astley, R. Sugimoto, G. Gabard, E. Norde, E.J. Grift, M. Bocquier, The Effect of Steady Flow Distortion on Mode Propagation in a Turbofan Intake. Presented at 20th AIAA/CEAS Aeroacoustics Conference, Atlanta, June 2014.
6. E.J. Brambley, N. Peake, Sound Transmission in Strongly Curved Slowly Varying Cylindrical Ducts with Flow, J. Fluid Mech. 596(2008), 387-412.
7. A.J. Cooper, N. Peake, Propagation of Unsteady Disturbances in a Slowly Varying Duct with Mean Swirling Flow. J. Fluid Mech. 445 (2001), 207-234.
8. A.J. Cooper, Effects of Mean Entropy on Unsteady Disturbance Propagation in a Slowly Varying Duct with Mean Swirling Flow, J. Sound Vib. 291(3-5)(2006), 367-384.
9. V. Pagneux, N. Amir, J. Kergomard, A study of wave propagation in varying cross-section waveguides by modal decomposition, part I: theory and validation, Journal of the Acoustical Society of America 100 (1996) 2034–2048.
10. S. Felix and V. Pagneux, Sound Attenuation in Lined Bends, J. Acoust. Soc. Am. 116 (4), Pt. 1, October 2004, 1921-1931.
11. S. Felix, A. Maurel, J-F. Mercier, Improved Methods for the Acoustic Propagation in Waveguides with Finite Wall Impedance. J. of Wave Motion, 54(2015) 1-10.
12. A. Maurel, J-F. Mercier, S. Felix, Propagation in Waveguides with Varying Cross Section and Curvature: a New Light on the Role of Supplementary Modes in Multi-Modal Methods. Proc Math Phys Eng Sci. / The Royal Society, 2014 Jun 8; 470(2166): 20140008.
13. J-F. Mercier, A. Maurel, Improved multimodal method for the acoustic propagation in waveguides with a wall impedance and a uniform flow, Proc Math Phys Eng Sci. / The Royal Society, 2016 Jun; 472(2190): 20160094.
14. E. J. Brambley, Well-Posed Boundary Condition for Acoustic Liners in Straight Ducts with Flow, AIAA Journal, Vol. 49, No. 6 (2011), pp. 1272-1282.
15. A.G. Wilson, A Method for Deriving Tone Noise Information from CFD Calculations on the Aeroengine Fan Stage. Presented at the NATO RTO-AVT Symposium on Computational Aero- and Hydro-Acoustics, 8-11 Oct. 2001, Manchester, UK.
16. A.G. Wilson, Application of CFD to Wake/Aerofoil Interaction Noise – A Flat Plate Validation Case. AIAA-2001-2135, presented at 7th AIAA/CEAS Aeroacoustics Conference, Maastricht, 28-30 May.
17. N.C. Ovenden, S.W. Rienstra, Mode-Matching Strategies in Slowly Varying Engine Ducts, AIAA Journal, Vol. 42, No. 9 (2004), pp. 1832-1840.
18. Kousen, K.A., Eigenmodes of Ducted Flows with Radially-Dependent Axial and Swirl Velocity

Components. NASA/CR 1999-208881 (1999).

19. P. Moinier, M. Giles, Eigenmode Analysis for Turbomachinery Applications. J Prop. Power 21, No. 6(2005), 973ff.
20. J.D. Anderson, Computational Fluid Dynamics, The Basics with Applications. McGraw-Hill International Editions, Mechanical Engineering Series, ISBN 0-07-113210-4, 1995.
21. A.L. Maldonado, J. Astley, P. Murray, G. Gabard, The Impact of Mean Swirling Flows on Sound Propagation in the Absence of Liners: a Parametric Study, Presented at the 23rd Int. Congress On Sound and Vibration, 10-14 July 2016, Athens, Greece.
22. S. Felix, V. Pagneux, Multimodal Analysis of Acoustic Propagation in Three-Dimensional Bends, Wave Motion 36 (2002) 157–168.
23. A.G. Wilson, Eigen Analysis in General Curvilinear Coordinates for Prediction of Noise Propagation in Aeroengine Inlets. AIAA-2017-3704, presented at 23rd AIAA/CEAS Aeroacoustics Conference, Denver, Colorado, 5-9 June 2017.
24. S.W. Rienstra, A. Hirschberg, An introduction to acoustics. Extended and revised edition of Report IWDE92-06, Technische Universiteit Eindhoven, 2001.
25. A.G. Prinn, R. Sugimoto, R.J. Astley, The Effect of Steady Flow Distortion on Noise Propagation in Turbofan Intakes. Presented at 22nd AIAA/CEAS Aeroacoustics Conference, Lyon, June 2016
26. J.T. Post, E.L. Hixson, A Modelling and Measurement Study of Acoustic Horns, Dissertation, Electroacoustics Research Laboratory, Dept. of Electrical and Computer Engineering, The University of Texas at Austin (1994).
27. B. Spain, Tensor Calculus (Third Edition). Oliver and Boyd Ltd, London, 1960.